Challenges in modelling spatiotemporally varying phytoplankton blooms in the Northwestern Arabian Sea and Gulf of Oman

S. Sedigh Marvasti[1], A. Gnanadesikan[2], A.A. Bidokhti[3], J.P. Dunne[4], S. Ghader[5]

[1] Department of Marine Sciences, Science and Research Branch, Islamic Azad University, Tehran, Iran. (safoora.seddigh@gmail.com)

[2] Department of Earth and Planetary Sciences, Johns Hopkins University, Olin Hall, 3400 N. Charles St., Baltimore, MD 21218, USA. (gnanades@jhu.edu)

[3] Institute of Geophysics, University of Tehran, Tehran, P. O. Box 14155-6466, Iran. (bidokhti@ut.ac.ir)

[4] National Oceanic and Atmospheric Administration/Geophysical Fluid Dynamics Laboratory, 201 Forrestal Rd., Princeton, NJ 08540-6649. (john.dunne@noaa.gov)

[5] Institute of Geophysics, University of Tehran, Tehran, P. O. Box 14155-6466, Iran. (sghader@ut.ac.ir)

Correspondence to: S. Sedigh Marvasti (safoora.seddigh@gmail.com)

Abstract

Recent years have shown an increase in harmful algal blooms in the Northwest Arabian Sea and Gulf of Oman, raising the question of whether climate change will accelerate this trend. This has led us to examine whether the Earth System Models used to simulate phytoplankton productivity accurately capture bloom dynamics in this region- both in terms of the annual cycle and interannual variability. Satellite data (SeaWIFS ocean color) shows two climatological blooms in this region, a wintertime bloom peaking in February and a summertime bloom peaking in September. On a regional scale, interannual variability of the wintertime bloom is dominated by cyclonic eddies which vary in location from one year to another. Two coarse (1°) models with the relatively complex biogeochemistry (TOPAZ) capture the annual cycle but neither eddies nor the interannual variability. An eddy-resolving model (GFDL CM2.6) with a simpler biogeochemistry (miniBLING) displays larger interannual variability, but overestimates the wintertime bloom and captures eddy-bloom

coupling in the south but not in the north. The models fail to capture both the magnitude of the wintertime bloom and its modulation by eddies in part because of their failure to capture the observed sharp thermocline/nutricline in this region. When CM2.6 is able to capture such features in the Southern part of the basin, eddies modulate diffusive nutrient supply to the surface (a mechanism not previously emphasized in the literature). For the model to simulate the observed wintertime blooms within cyclones, it will be necessary to represent this relatively unusual nutrient structure as well as the cyclonic eddies. This is a challenge in the Northern Arabian Sea as it requires capturing the details of the outflow from the Persian Gulf-something that is poorly done in global models.

1   Introduction

The region of northwestern Arabian Sea and the Gulf of Oman (15°–26° N, 56°–66°E) is a highly productive region (Madhupratap et al., 1996; Tang et al., 2002), with satellite estimates of carbon export of 137 gC/m^2/yr, much higher than the ~80 gC/m^2/yr found in the Subpolar North Atlantic and Pacific (Dunne et al., 2007). Peak chlorophyll-a concentrations exceed 0.7 mg/m^3 in this region (Fig. 1a).

This region may be changing in important ways. In both the Persian Gulf and the Gulf of Oman, there is evidence that harmful algal bloom (HABs) and their impacts are increasing (Richlen et al., 2010). HAB occurrences have been more frequently reported in the Gulf of Oman than in the Persian Gulf. A total of 66 red tide events (mostly dominated by *Noctiluca scintillans*) have been recorded between 1976 and 2004 including 25 blooms resulting in mass mortality of fish and marine organisms. Reasons for the increase in blooms include aquaculture, industrial and sewage inputs, natural dispersal and human-aided transport, long-term increases in nutrient loading and global expansion of species (Richlen et al., 2010) as well as global climate change (Goes et al., 2005). The latter paper suggested that increasing blooms were driven by an increase in the strength of the Asian monsoon.

Evaluating such a possibility and extending it into the future requires the use of Earth System Models. However, such projections will only be as good as the models on which they are based. In this paper we examine several models run at the Geophysical Fluid Dynamics Laboratory in the Arabian Sea. We consider numerical results from five different 3D global Earth system models, which we denote CORE-TOPAZ, Coupled-TOPAZ, Coupled-BLING, Coupled-miniBLING, and the Geophysical Fluid Dynamics Laboratory Climate Model

2

62 version 2.6 (CM2.6 miniBLING). The first two of these models use the relatively complex
63 TOPAZ biogeochemistry, but have low resolution and do not resolve eddies, the third has a
64 simplified biogeochemistry (BLING, Galbraith et al., 2010) which does not carry
65 phytoplankton biomass as a separate variable while the last two models have an even simpler
66 biogeochemistry that does not directly simulate dissolved organic matter or iron cycling
67 (miniBLING, Galbraith et al., 2015b). Only the final model resolves eddies.

68   The seasonal cycle is an important metric for models to be able to simulate. The
69 Arabian Sea is influenced by a reversing monsoonal cycle (Wang and Zhao, 2008), an
70 evaporative fresh-water flux over most of the basin, and an annual mean heat gain (Banse and
71 McClain, 1986; Fischer et al., 2002). In summer (June-September), the southwest Monsoon
72 (SWM) blows strongly across the northwestern Arabian Sea (Al-Azri et al., 2010). Driven by
73 a land-sea pressure gradient, the SWM is a large-scale feature of the atmospheric circulation
74 of the tropics, extending from a surface pressure high near 30° S in the southern hemisphere
75 northward to the surface low over Asia (Anderson and Prell, 1993). During the SWM, winds
76 are steered by the East African highlands to form a strong low level atmospheric jet, referred
77 to as the Findlater Jet (Bartolacci and Luther, 1999; Honjo et al., 2000), which crosses the
78 Equator over the Indian Ocean and blows over the Arabian Sea parallel to the Omani
79 coastline in a northeast direction (Honjo et al., 2000). The orientation of the Findlater Jet
80 parallel to Omani coast leads to coastal upwelling along the coast and downwelling on the
81 eastern side of the Jet in the middle of Arabian Sea. This upwelling provides nutrients to the
82 surface layer (Fig. 1b) (Al-Azri et al., 2013; Kawamiya and Oschlies, 2003; Madhupratap et
83 al., 1996; Murtugudde et al., 2007; Veldhuis et al., 1997; Wang and Zhao, 2008). The SWM
84 does not destabilize the surface layers, which are fairly stable in northern summer (Fig. 1c).

85   The Northeast Monsoon (NEM), which happens from December through February, is
86 not as strong as the SWM (Dickey et al., 1998; Shalapyonok et al., 2001; Veldhuis et al.,
87 1997). Ocean surface wind stress is lower (0.032 N/m^2 in NEM compared to 0.127 N/m^2 in
88 SWM), and does not lead to upwelling like the SWM along the Omani coast. However,
89 negative heat flux results in a destabilizing buoyancy flux, subsequent convective overturning
90 (Barimalala et al., 2013; Kawamiya and Oschlies, 2003), and deepening and cooling to a
91 depth of ~60m (Fig. 1c, 1d). This brings up nutrients and fuels a wintertime bloom. In
92 addition, as shown in Fig. 1d in wintertime bloom the mixed layer depth (MLD) is deeper
93 than summer.

94   A second metric of the bloom dynamics is the relationship between the blooms and
95   mesoscale eddies (Al-Azri et al., 2013; Dickey et al., 1998; Hamzehei and Bidokhti, 2013;
96   Shalapyonok et al., 2001; Gomes et al., 2005). The confluence of the Persian Gulf outflow
97   current and the East Arabian Sea Current parallel to Omani and Yemeni coastlines in Arabian
98   Sea leads to formation of a frontal zone and formation of persistent eddies in the region.
99   Because the size of eddies is comparable to the width of the Gulf of Oman, they can affect
100   mixing and transport of biota on a basin scale (Fischer et al., 2002; Piontkovski et al., 2012).
101   Piontkovski et al. (2012) suggested that the increased amplitude of the seasonal cycle of
102   chlorophyll-a might be associated with the increased variability of mesoscale eddy kinetic
103   energy (EKE) per unit mass in the Gulf of Oman or in the western Arabian Sea. Gomes et al.
104   (2008) noted potential anticorrelation between sea surface height and chlorophyll, but did not
105   find a consistent relationship over time.

106   Gaube et al. (2014) provide a global overview of how eddies influence chlorophyll
107   blooms. They find that the effect of mesoscale eddies on the chlorophyll bloom varies both
108   temporally and spatially. They identify four particular mechanisms that can be distinguished
109   by linking sea surface anomalies to chlorophyll, namely eddy stirring, trapping, eddy
110   intensification, and Ekman pumping. Although Gaube et al. (2014) find a negative correlation
111   between chlorophyll and SSH in the Arabian Sea, they do not analyse which of these
112   mechanisms is involved in this region, nor do they quantify the extent to which this
113   correlation varies over the course of the season.

114   Resplandy et al. (2011) indicated that the spatial variability associated with mesoscale
115   eddies in the Arabian Sea produces spatial variability in the bloom and that another source of
116   variability is found to be restratification at these structures. Advection from coastal region is
117   identified as the mechanism providing nutrients in summer, while vertical velocities
118   associated with mesoscale structure are found to increase the overall nutrient supply.
119   However, this work does not make clear how the spatial distribution of the eddy nutrient
120   supply is related to the eddies, not whether this relationship is the same in all seasons.

121   The structure of this paper is as follows: all datasets including ocean color data and
122   altimeter data are explained in section 2 of the paper along with the specification of five
123   different 3D global Earth system models. In section 3, the remote sensing results are used to
124   study the spatiotemporal variability of chlorophyll-a in mesoscale structures in the study
125   region. We find a seasonal relationship between SSHA and chlorophyll such that cyclonic

126 eddies are associated with blooms, but only during the winter. This means that interannual
127 variability in blooms will be shaped by mesoscale eddy activity and may not be predictable.
128 Results of the 3D global Earth system models are discussed in section 4. Annual cycles of
129 variation of chlorophyll-a and nutrients for all GFDL models within the whole region are
130 compared against the corresponding satellite results and field measurements. The models tend
131 to overestimate wintertime productivity, in large part due to excessive mixing. They also fail
132 to explain the bloom-SSHA relationship except in a few special cases. We argue that the
133 eddies act to modulate turbulent mixing of nutrients to the surface- a mechanism not
134 emphasized in previous literature. However, this can only occur if there is a strong and
135 relatively shallow nutricline. Since the model only simulates such a feature in the Southern
136 Arabian Sea, it does not capture the observed relationship between SSH and biology. Both the
137 overestimation of the wintertime bloom and the failure to predict its modulation by eddies can
138 thus be traced to difficulties in modeling the stratification of the Northwest Arabian Sea, most
139 likely as a result of a failure to properly simulate overflows.

140

141 **2   Description of data and models**

142 **2.1   Satellite products**

143 We examine the relationship of blooms and eddies using the GSM5 Maritorena et al. (2002)
144 product based on the SeaWIFS (Sea-viewing Wide Field-of-view Sensor) ocean color data
145 and Sea Surface Height Anomaly (SSHA), based on altimeter data acquired from the
146 Archiving, Validation and Interpretation of Satellite Oceanographic (AVISO) Data Center
147 (http://www.aviso.oceanobs.com). The SSH anomaly is calculated relative to the annual
148 cycle.

149 The GSM algorithm represents the normalized water leaving radiance $L_{wN}(\lambda)$ at multiple
150 wavelengths as a nonlinear function, as following (Maritorena et al., 2002),

151
$$\hat{L}_{wN}(\lambda) = \frac{tF_0(\lambda)}{n_w^2} \sum_{i=1}^{2} g_i \left\{ \frac{b_{bw}(\lambda) + b_{bp}(\lambda_0)(\lambda/\lambda_0)^{-\eta}}{b_{bw}(\lambda) + b_{bp}(\lambda_0)(\lambda/\lambda_0)^{-\eta} + a_w(\lambda) + Chl\, a_{ph}^*(\lambda) + a_{cdm}(\lambda_0)exp[-S(\lambda-\lambda_0)]} \right\}^i \quad (1)$$

152 where t is the sea–air transmission factor, $F_0(\lambda)$ is the extraterrestrial solar irradiance, n_w is the
153 index of refraction of the water, seawater backscatter $b_{bw}(\lambda)$, absorption $a_w(\lambda)$, a_{ph}^* is the
154 chlorophyll-a (*chl*) specific absorption coefficient, S is the spectral decay constant for

155 absorption by chromophoric dissolved organic materials (CDOM), η is the power-law

156 exponent for the particulate backscattering coefficient, and λ_0 is a scaling wavelength (443

157 nm). The cdm absorption coefficient [$a_{cdm}(\lambda_0)$], and slope factor S then determine the

158 absorption across a range of wavelengths while the particulate backscatter coefficient [$b_{bp}(\lambda_0)$]

159 and coefficient η constrain the scattering. Letting λ_0 be 443 nm assuming that all terms other

160 than *chl*, [$a_{cdm}(\lambda_0)$] and b_{bp}(443nm) are constant, one can then use the normalized water

161 leaving radiance to invert for *chl*, a_{cdm}, and backscatter b_{bp}. One limitation of this approach is

162 that if the inherent optical properties vary with time or space, this variation will introduce

163 errors into the estimate. Following Behrenfeld et al. (2005), we convert the backscatter

164 coefficient into units of particulate carbon biomass using the relationship *p_{carb}=13000(b_{bp}-*

165 *0.00035)*.

166 Satellite-based remote sensing is the only observational method suitable for measuring

167 physical and biological properties over large regions of the ocean. However, satellite ocean

168 color and SST are limited to surface distributions and provide no information about the

169 vertical structure within the ocean (McGillicuddy et al., 2001). Additionally acquiring data

170 requires cloud-free viewing of the ocean surface, which as we will see is a problem in this

171 region at certain times of the year. This lack of information motivates our examination of

172 numerical models, which ideally could be used to provide estimates of the ocean state when

173 observations are sparse as well as to extrapolate both vertically and into the future.

174

175 **2.2 Numerical models**

176 Numerical results are presented in this paper based on the output of five different 3D

177 global Earth system models, which we denote CORE-TOPAZ, Coupled-TOPAZ, Coupled-

178 BLING/miniBLING and GFDL CM2.6 (miniBLING). The first two of these models use the

179 relatively complex TOPAZ biogeochemistry, but have low resolution and do not resolve

180 eddies. The third and fourth use two simplified biogeochemistry codes (BLING and

181 miniBLING) which do not carry phytoplankton biomass as a separate variable while the last

182 model has very high resolution and uses the miniBLING simplified biogeochemistry. Below,

183 we describe the different physical models, followed by a summary of the biogeochemical

184 codes run within these models.

185

186   2.2.1 Physical model description

187   The ocean-ice model used in the CORE-TOPAZ model follows the corresponding
188   components of the GFDL CM2.1 global coupled climate model (Delworth et al., 2006). The
189   vertical resolution ranges from 10 m over the top 200 m to a maximum thickness of 250 m at
190   5500 m depth with 50 layers in all. The meridional resolution is 1°, whereas the zonal
191   resolution varies between 1° in mid-latitudes and $1/3^o$ at the equator. North of 65°, a tripolar
192   grid is employed to avoid singularity arising from convergence of meridians at the North
193   Pole. Up-to-date parameterizations of mixed-layer dynamics, isopycnal mixing, advection by
194   subgridscale eddies, bottom topography, bottom flows, and lateral viscosity are included- for
195   more detail see Griffies et al. (2005) and Gnanadesikan et al. (2006). Both the dynamics and
196   thermodynamics sea ice are simulated with of five thickness classes of sea ice being resolved.

197   In the CORE-TOPAZ model, surface forcing is set using the Coordinated Ocean-ice
198   Reference Experiment (CORE) protocol (Griffies et al., 2009), where the inputs for
199   calculating surface fluxes are taken from an atmospheric analysis dataset adjusted to agree
200   better with in situ measurements. Sensible and latent heat fluxes are then calculated using
201   bulk formulae. Freshwater forcing is given by a combination of applied precipitation,
202   evaporation computed using bulk fluxes, and a correction diagnosed to restore surface
203   salinities in the top 10 m to climatological monthly values over 60 d. Hence, the fluxes
204   forcing the CORE runs could be thought of as "best guess" observationally based estimates.
205   Such a prescription omits important feedbacks whereby the atmosphere ensures that rainfall
206   and evaporation are consistent with each other, although the restoring correction is a crude
207   representation of these feedbacks. We use the version of the model described in Gnanadesikan
208   et al. (2011), which analyzed different modes of interannual variability in biological cycling
209   across the North Pacific Ocean.

210   The Coupled-TOPAZ model corresponds to the control simulation of the GFDL
211   ESM2M submitted as part of the IPCC AR5 process (Dunne et al., 2012). In this model the
212   ocean is coupled to the atmosphere, land, and sea ice components. Gnanadesikan et al. (2014)
213   discuss the behavior of this model in the North Atlantic, but its behavior in the Arabian Sea
214   has not been previously analyzed. Two additional versions of this model, referred to here as
215   Coupled-BLING/miniBLING, were run using the BLING and mini-BLING biogeochemical
216   models described below, but with the light field given by the TOPAZ code. The differences
217   between the 1-degree models highlight differences due to biological formulation.

218　　　　The ocean component of ESM2M employs the MOM4p1 code of Griffies et al. (2009)

219　　which largely mimics the CM2.1 ocean (identical horizontal and vertical resolution and

220　　parameterization of mixing). However, ESM2M ocean uses a rescaled geopotential vertical

221　　coordinate ($z*$; Adcroft et al., 2004; Stacey et al., 1995) for a more robust treatment of free

222　　surface undulations. The ESM2M implementation includes updates to the K-profile

223　　parameterization (Large et al., 1994) based on Danabasoglu et al. (2006), as well as model-

224　　predicted chlorophyll modulation of short-wave radiation penetration through the water

225　　column. ESM2M also includes completely novel parameterizations relative to CM2.1, such as

226　　parameterization of submesoscale eddy-induced mixed layer restratification (Fox-Kemper et

227　　al., 2008). Instead of prescribed vertical diffusivity for interior mixing (Bryan and Lewis,

228　　1979), ESM2M employs the Simmons et al. (2004) scheme along with a background

229　　diffusivity of 1.0×10^{-5} m^2 s^{-1} in the tropics and 1.5×10^{-5} m^2 s^{-1} poleward of 30° latitude

230　　following a *tanh* curve.

231　　　　The Geophysical Fluid Dynamics Laboratory Climate Model version 2.6 (CM2.6) is a

232　　high-resolution eddy-resolving model. This model has the same atmosphere model and ocean

233　　Physics as CM2.5 (Delworth et al., 2012). CM2.6's ocean component has higher horizontal

234　　resolution than CM2.5, with grid spacing, which is changeable from 11 km at the equator to

235　　less than 4 km at very high latitudes. This means that the model is capable of resolving eddy

236　　features in the tropics, as we will see below.

237

238　　2.2.2 Biogeochemical Cycling codes

239　　　　The TOPAZ code (Tracers of Ocean Productivity with Allometric Zooplankton code

240　　of Dunne et al., 2010), keeps track of five inorganic nutrients used by phytoplankton: nitrate

241　　and ammonia, inorganic phosphate, silicate, and dissolved iron. Additionally, the model

242　　carries three other dissolved inorganic tracers: dissolved inorganic carbon, alkalinity and

243　　dissolved oxygen. Based on the work of Dunne et al. (2007), the model also keeps track of

244　　fine lithogenic material, which plays a role in ballasting organic material and delivering it to

245　　the sediment (Armstrong et al., 2002; Klaas and Archer, 2002). The five inorganic nutrients

246　　are taken up in different ways by three classes of phytoplankton: small, large and

247　　diazotrophic. A comprehensive description of TOPAZ v2 can be found in the supplemental

248　　material of Dunne et al. (2013).

249   TOPAZ is unusual among comprehensive Earth System Models in that it uses a highly
250   parameterized version of grazing. Instead of grazers being explicitly simulated, grazing rates
251   are simply taken as a function of phytoplankton biomass, with different power-law
252   dependence for small and large phytoplankton. The grazing formulation was fit to about 40
253   field sites to produce a size structure that transitions realistically between being dominated by
254   small phytoplankton and low particle export ratio at low levels of growth and large
255   phytoplankton and high particle export ratio in nutrient and light-replete conditions. At
256   equilibrium, the resulting parameterization produces biomass that is a function of growth rate
257   (linear for small plankton, cubic for large). A similar scaling in particle size spectrum was
258   seen across ecosystems by Kostadinov et al. (2009). In contrast to models that explicitly
259   simulate zooplankton, TOPAZ does not depend on poorly known zooplankton behavioral
260   parameters (such as handling efficiency or grazing half-saturation) or on the details of how
261   different trophic levels interact.

262   Even though it does not simulate zooplankton explicitly, TOPAZ still carries over two
263   dozen tracers, making it extremely expensive to run in high-resolution simulations. For this
264   reason Galbraith et al. (2010) developed the Biogeochemistry with Light Iron Nutrients and
265   Gasses (BLING) model, which parameterizes the entire ecosystem. The original version of
266   BLING has only five explicit tracers: dissolved inorganic phosphorus (PO_4), dissolved
267   organic phosphorus (DOP), dissolved Iron (Fe), dissolved inorganic carbon (DIC), and
268   oxygen (O_2). It includes the impacts of macronutrient and micronutrient limitation and light
269   limitation on phytoplankton by using these to calculate a growth rate. Using the same
270   machinery as TOPAZ, it then uses this growth rate and implicit treatment of community
271   structure to estimate phytoplankton biomass, and uses this biomass to calculate the rate at
272   which nutrient is taken up by plankton and cycled through the ecosystem.

273   The miniBLING code (Galbraith et al., 2015) represents a further simplification. In
274   this model the iron field is taken from a lower-resolution version of the model (an
275   approximation which has limited impact in the Arabian Sea, where phytoplankton are
276   generally not iron-limited) and so Fe is not treated prognostically. Additionally the DOP pool
277   is eliminated. Simulations using the ESM2M physical model show that control simulations of
278   oxygen and surface nutrients produced by the miniBLING and BLING models are very
279   similar to those produced in the same model with TOPAZ (Galbraith et al., 2015). Galbraith
280   et al. (2015) also show that BLING and miniBLING simulate very similar patterns of oxygen

281 change and anthropogenic uptake in a simulation where CO2 is increased by 1% per year

282 until it is twice the preindustrial concentration.

283   It should be noted that simplified BLING and miniBLING codes neglect some

284 processes that may be important. Only nonliving components are advected and mixed by the

285 ocean circulation, which could result in inaccurate distribution of biology in frontal regions at

286 high resolution. Additionally, as will be discussed below, the lack of a biomass variable may

287 lead to overestimating how rapidly plankton inventories can grow. Also, the rich behavior of

288 the nitrogen cycle with its interaction with iron, phosphorus and oxygen cannot be simulated

289 with one macronutrient tracer (Behrenfeld 2010). Specifying iron limitation, as done in

290 miniBLING, may also have some impacts in our region. As extensively discussed by Naqvi et

291 al., (2010) there is a possibility of iron limitation over the southern parts of the Omani shelf

292 and in the offshore region during the latter part of the Southwest Mansoon, which can result

293 in high nitrate-low chlorophyll conditions. The western equatorial and southern tropical

294 region of the Indian Ocean are iron-limited and the Arabian Sea (southern parts) may become

295 iron-limited under strong upwelling conditions (Wiggert et al., 2006).

296

297 **3   Remote sensing results**

298 **3.1   Annual cycle and interannual variability**

299 We begin by using the GSM5 satellite data to examine the annual cycle and interannual

300 variability in two different regions, the whole NW Arabian Sea (56°-66° E, 15°-26° N) and a

301 smaller region including the Gulf of Oman, (60°-62° E, 22°-26° N). As shown in Fig. 2 (a) to

302 (c) for whole region, clear annual cycles of chlorophyll-a, backscattering and CDOM are

303 observed. Even larger annual cycles of variation of chlorophyll-a, backscattering and CDOM

304 are seen in the smaller region, as shown in Fig. 2 (d) to (f). More pronounced interannual

305 variability is observed in the smaller region as opposed to the larger region.

306 The annual variations of all parameters are broadly consistent with each other. The maximum

307 values associated with the summer bloom are generally seen in September, with values of 1.0

308 mg/m^3, 50 mgC/m^3, and 0.1 m^{-1} for chlorophyll, particulate carbon and CDOM, respectively,

309 within the whole region. Within the smaller region, the values are 1.25 mg/m^3, 65 mgC/m^3,

310 and 0.125 m^{-1} for chlorophyll, particulate carbon, and CDOM, respectively. For two years of

311 2001 and 2002, the particulate carbon values (~90 mgC/m^3) are much higher that the average

312 of the other months over both regions, but the chlorophyll does not show pronounced peaks.

313 A winter bloom is also pronounced in February as a second maximum in a yearly cycle,

314 where the magnitudes are about 0.07 mg/m^3, 40 mgC/m^3, and 0.07 m^{-1} for chlorophyll,

315 particulate carbon and CDOM, respectively, within the whole region, and about 0.09~1.5

316 mg/m^3, 55~80 mgC/m^3, and 0.11~0.14 m^{-1} for chlorophyll, particulate carbon and CDOM,

317 respectively, within the smaller region. That the summer bloom in the both regions is stronger

318 than the winter bloom has been discussed by Al-Azri et al. (2010), and Levy et al. (2007).

3.2 Variability of Chlorophyll-a in Mesoscale Structures

320 Mesoscale structures can be seen in the Northwest Arabian Sea in both the SeaWiFS

321 chlorophyll-a distribution and AVISO sea surface height anomaly. Over the course of 2001

322 (Fig. 3), both a summer bloom (which most likely starts in August and ends in ~October) and

323 a winter bloom (which starts in January and goes away in April) can be seen in chlorophyll-a.

324 In March, the last month of the winter bloom, chlorophyll-a concentrations are high over the

325 entire region in both the anticyclones (warm eddies with positive SSHA) and the cyclones

326 (cold eddies with negative SSHA). The observed bloom in March terminates abruptly in

327 April, although the observations show that eddies are still active in the region. In June, July

328 and August, the satellite ocean color data is not available due to excessive cloudiness. In

329 September, the last month of the summer bloom, most of the region including cyclones and

330 anticyclones and coastal regions had high chlorophyll-a concentration. However in the

331 following months the bloom persists only within the cold eddies and disappears over the

332 warm eddies (a phenomenon also seen in Sargasso Sea by McGillicuddy et al., 2001). The

333 relationship between sea surface chlorophyll-a and eddies for the other years between 1998

334 and 2005 during the month of November, is shown in Fig. 4. The relationship between

335 blooms and SSHA is clear and striking. Note particularly the difference between 1998 and

336 2001, when the location of high and low chlorophyll regions switches relative to the Ras al

337 Hadd. This difference in bloom location is perfectly reflected in the different locations of the

338 eddies.

3.3 Chlorophyll-Sea Surface Height Anomaly (SSHA) cross-correlation

340 The seasonal relationship between chlorophyll and SSHA can be seen in the monthly

341 variation of the spatial cross-correlation between the two variables over the entire northwest

342 Arabian Sea. chlorophyll-SSHA cross-correlations between 1998 and 2005 in the satellite

343   data are shown in Fig. 5a. To check that the chlorophyll results are not an artifact of the
344   remote sensing inversion, two other related parameters, the backscattering coefficient (BBP)
345   and chromophoric dissolved organic matter (CDOM) are also cross-correlated with SSHA, as
346   depicted in Figs. 5b and c. The results show consistent annual cycles of variation in the cross-
347   correlation of all three variables. This suggests a repeatable yearly phenomenon in the region
348   as discussed in the previous sections. The cross-correlation results over the 8 years of study
349   show that there are several months (i.e. November-December) with relatively high anti-
350   correlation for most of the years and also several other months (i.e. April-May) with no or
351   even low positive correlation.

352   The averaged climatological monthly cross-correlation with SSHA and climatological
353   monthly values between 1998 and 2005 are shown in Fig. 6 for all parameters. Two blooms
354   ending in March (winter) and September (summer) are seen. At the peak of the blooms the
355   average cross-correlation values are very low due to the existence of blooms in both cyclones
356   and anticyclones. The months after the winter and summer blooms show a clear difference in
357   the correlation. After the winter bloom (typically April and May), the cross-correlation is
358   positive or very small, which suggests no relation between the mesoscale eddies and the
359   blooms. As discussed in Kumar et al. (2001), low primary production is observed after
360   termination of winter cooling during Spring Inter-Mansoon (SIM) (see also Gomes et al.,
361   2008). This result would be also consistent with SIM producing weak atmospheric forcing in
362   the region.

363   In contrast, after the summer bloom (typically October-December) as the average values of
364   chlorophyll-a decrease, chlorophyll and SSHA become relatively highly anti-correlated. The
365   reason for the anti-correlation is the persistence of chlorophyll at the regions with negative
366   SSHA that are typically considered to be cyclonic (cold) eddies and disappearance of
367   chlorophyll-a in positive SSHA that are assumed to be anti-cyclonic (warm) eddies. Particle
368   backscatter also provides almost same cross-correlation suggesting that the chlorophyll-a
369   signal does not result purely from photo-adaptation. Moreover, the CDOM-SSHA cross-
370   correlation shows the same annual cycle although with smaller peak values.

371   The spatial relationship between blooms and eddies seen in the Northern Arabian Sea can be
372   compared with the patterns noted by Gaube et al. (2014). Their eddy stirring mechanism
373   involves advection of high and low chlorophyll signals around an eddy, resulting in a low
374   which is offset from the center of an anticyclone and a high which is offset from the center of

375 a cyclone. Ekman pumping would be expected to produce negative anomalies in cyclones

376 with a positive "halo" and positive anomalies in anticyclones with a negative "halo" (Gaube

377 et al. (2014), Fig. 2). Trapping of chlorophyll involves eddies retaining the properties that

378 they had when shed from a boundary current, which would generally imply low values in

379 anticyclones and high values in cyclones. Eddy intensification would be expected to produce

380 the same picture, as cyclones would see rising nutriclines in the center but anticyclones would

381 see deepening nutriclines. The basic picture seen in the Arabian Sea is inconsistent with the

382 first two mechanisms but is potentially consistent with the second two. However, without in-

383 situ data it is impossible to validate either of these mechanisms.

384

385 **4   Numerical modelling results**

386 **4.1   Temporal variability**

387 Time series of chlorophyll-a , phosphate and nitrate for all GFDL models are shown in Fig. 7a

388 to c within the whole region and compared against the corresponding GSM5 satellite results

389 or WOA09. Note that the eight years of the model output, selected as the last eight years of

390 the run, would not be expected to correspond to the eight actual years in the satellite data. The

391 annual cycles of chlorophyll-a and biomass are quite similar to each other in all GFDL

392 models, insofar as they show two distinct blooms in yearly cycle. The maximum values that

393 can be considered as a winter bloom in the whole region are mostly seen around February

394 (Piontkovski et al., 2011), with values of 0.32–0.38, 0.48–0.62, 1.0–2.0, 1.5-2.2, 0.8-1.6, and

395 0.6-0.75 mgm^{-3} for chlorophyll in CORE-TOPAZ, Coupled-TOPAZ, CM2.6 (miniBLING),

396 miniBLING (Low resolution), BLING and satellite data, respectively. A summer bloom is

397 also pronounced in September as a second maximum in the yearly cycle over the whole

398 region, with peak magnitudes of about 0.25-0.52, 0.65–0.7, 0.65-1.15, 0.8-1.15, 0.5-0.75, and

399 0.75-1.3 mgm^{-3} for chlorophyll across the different datasets.

400 Notice the results from the BLING model run in the coarser resolution ESM2M code (purple

401 lines). The differences between BLING and miniBLING (light blue lines) in this code are just

402 due to having fixed iron and no dissolved phosphorus in miniBLING. The light field in these

403 ESM2M runs is computed from using TOPAZ-derived chlorophyll, so that all three models

404 see identical physical conditions. Both BLING and miniBLING in ESM2M produce an

405 asymmetry in chlorophyll between February and September that is similar to that produced in

13

406 CM2.6 miniBLING. This asymmetry is not seen in TOPAZ. Analysis of what drives this
407 asymmetry shows that it is not straightforward. All of the model runs show an asymmetry in
408 the nutrient concentrations that is in the opposite direction as the observations, with higher
409 nutrients in February than in September, as shown in Fig 7b. As we will show later in the
410 manuscript, this is probably associated with the models mixing to excessive depth during the
411 wintertime. However, in TOPAZ this does not produce an asymmetry in chlorophyll, while in
412 BLING and miniBLING it does. There are two possible reasons for this:

413 1) The equilibrium assumption, which means that biomass in both BLING and miniBLING is
414 not directly simulated. In TOPAZ, the growth of plankton during the spring is limited by the
415 biomass of phytoplankton, whereas in the fall TOPAZ continues to have higher heterotrophic
416 biomass (diagnosed from growth rates over previous months) that then grazes the plankton. In
417 BLING and miniBLING, by contrast, the biomass responds almost instantaneously to changes
418 in growth conditions. This means that if the growth rate increases from 0.05 day^{-1} to 0.1 day^{-1}
419 over the course of a month, the biomass associated with large phytoplankton will increase
420 eightfold, even though the additional growth should only be enough to give an increase of a
421 factor of 30 days×0.05 day^{-1}=1.5. Possibilities for addressing this effect include replacing the
422 DOP tracer with a biomass tracer, which could then partitioned between the different
423 phytoplankton boxes based on the temporally smoothed growth rate, or increasing the
424 timescale over which the growth rate is smoothed when biomass is calculated.

425 2) Different handling of light limitation. In TOPAZ light limitation is calculated using the
426 instantaneous local light, whereas in BLING it is calculated using the mixed layer average
427 light. Preliminary results with a very coarse resolution model using BLING show that this
428 reduces the summer-winter asymmetry slightly, but is not sufficient to make the February
429 bloom smaller than the September bloom. This effect will also be addressed in future
430 research.

431 It is likely that all three of these factors- too deep winter mixed layers leading to too high
432 nutrients, too little light limitation and instantaneous response to changes in growth
433 conditions, are all responsible for the overly strong blooms in boreal winter in the Arabian
434 Sea.

435 To get a better sense of the mechanisms driving the blooms in the model, the biomass (mol P
436 kg^{-1}) of the miniBLING CM2.6 model is compared with the light intensity in the mixed layer
437 and the light-saturated photosynthesis rate (carbon specific) (s^{-1}) in Figs. 8a and b for January

438   of year 195. The two terms in Fig. 8 are the two terms in the model that affect growth rate.

439   Because biomass in the miniBLING model is a function of growth rate only, understanding

440   the variation in two terms is sufficient to understand what drives the variation of biomass in

441   the model. The biomass production and mixed layer light intensity (Fig. 8a) are not

442   meaningfully correlated parameters. On the other hand, the biomass and the light-saturated

443   carbon specific growth rate (Fig. 8b; indicating the degree of nutrient limitation) are

444   positively correlated. From this, it can be concluded that the blooms in this region are more

445   driven by nutrient rather than light, consistent with, for example, Gomes et al. (2008). This

446   suggests in turn that it is likely biases in nutrient supply that drive biases in productivity.

447   We can get more insight into nutrient biases by examining the individual tendency terms

448   associated with advection, vertical diffusion and subgridscale eddy fluxes and time rate of

449   change of nutrients. For simplicity, in this paper we combine the vertical diffusive flux

450   associated with small-scale mixing from the background diffusion with that due to the mixed

451   layer parameterization. Fig. 9 shows PO_4 advection, diffusion and time tendency flux terms

452   for the whole region (56°-66^oE, 15°-26^oN) over a typical year. We calculate these by

453   integrating the time tendency terms for phosphate over the top 50m. The results show that the

454   dominant source in whole region during the winter bloom is diffusion, suggesting the model

455   predicts excessively strong mixing during the wintertime. By contrast, the advection

456   dominates diffusion during the summer bloom, supplying the majority of nutrients during the

457   months of July and August. The fact that the summertime bloom is close to observations

458   suggests that the model correctly simulates this wind-driven upwelling.

459   In addition to having annual cycles that are different from observations, the models also differ

460   from data in terms of interannual variability. As shown in Fig. 10, low-resolution models

461   (CORE- and coupled-TOPAZ) provide an almost uniform seasonal coefficient of variation

462   (mean C.o.Vs are 0.15 and 0.18, respectively), while both data and eddy resolving CM2.6

463   models show higher interannual variability and seasonal changes (mean C.o.Vs are 0.35 and

464   0.5, respectively). The C.o.Vs are particularly higher during the winter and summer blooms in

465   the observations, while the low-resolution models do not see these signals. In other words, the

466   low-resolution models fail to get enough variability, while the high-resolution models produce

467   too much interannual variability. Together with the Fig. 4, this statistical analysis suggests

468   that eddies are necessary to explain the variability in the data as opposed to the low-resolution

469　models, but that the high-resolution model does not properly capture this variability. Below,
470　we examine the relationship of eddies and blooms in the high-resolution models.

471

4.2　Blooms and sea surface height in CM2.6

4.2.1　Large-scale correlation

474　The relationship between SSHA and chlorophyll is quite different in the model as compared
475　to the satellite. Monthly variation in the cross-correlation of chlorophyll and SSHA for eight
476　consequent years in CM2.6 is shown in Fig. 11. As in the remote sensing, the model shows
477　annual cycles of variation in the cross-correlation, suggesting a repeatable yearly phenomenon
478　in the region. However the structure of this annual cycle is not consistent with the satellite
479　data. The model predicts several months (i.e. March-August) with anti-correlation for most of
480　the years, but with values less than 0.5, smaller than the peak anti-correlation values in
481　satellite results. The model also predicts that several other months (i.e. October-February)
482　should have no or even positive correlation, while the satellite shows strong negative
483　correlations during these months.

484

4.2.2　Blooms in Mesoscale Structures

486　Why does the GFDL CM2.6 model not produce the same relationship between SSHA and
487　chlorophyll as the satellite? We can gain some insight by examining snapshots of the two
488　fields. In Figs. 12a and b, sea surface chlorophyll-a concentration and sea surface height
489　anomaly (SSHA) are shown at two snapshots of time, November 9th and December 28th for
490　model year 195. Comparing the figures with the corresponding satellite results in Fig. 3 for
491　the months of November and December, we see that the southern part of the GFDL model is
492　more similar to the satellite data, with high concentrations of chlorophyll-a tending to be
493　located at the center of cyclones. In contrast, in the northern part of the region, the GFDL
494　model predicts high chlorophyll at the edges of the cyclones as well as in the center of
495　anticyclones. The eddy structures have smaller diameters in GFDL results than the field
496　observations, though it is not clear whether this represents smoothing in the AVISO product
497　or some physical weakness of the model.

498   We now focus on the few examples in our model output where chlorophyll blooms are found

499   in the center of cyclonic eddies. These are denoted as E1 and E2 in Figs. 12a and b. To track

500   the movement of the selected eddies, E1 and E2, over the time from November 9th to

501   December 28th, modeled chlorophyll and SSHA are shown in Figs. 12c and d along two

502   different latitudes, 16°N (for E1) and 19°N (for E2). Fig. 12c shows that E1 moved westward

503   during this period of time, and that the chlorophyll concentration was kept high within the

504   central part of the eddy. E1 appears to be created by the passage of a cyclone, similar to the

505   eddy observed by Wang and Zhao (2008) in the aftermath of Cyclone Gonu. Similarly, as

506   shown in Figs. 12d, E2 was a persistent eddy with both central and edge blooms during the

507   month of November that started to move towards the west during the December along 19°N.

508   However, at other latitudes, the largest blooms offshore are found along gradients in SSH

509   rather than being associated with maxima or minima. This suggests a different mechanism for

510   producing blooms in the model. Following Gaube et al. (2014). it appears that the eddy

511   stirring mechanism is dominant. Satellite data (i.e. see Fig. 3 for the month of May) provide

512   some hints of high-chlorophyll plumes being advected away from coastal regions. As shown

513   in Figs. 12a and b, high velocities in the marginal region between adjacent cyclonic and

514   anticyclonic eddies can cause such plumes in the GFDL models as well.

515   Why is the model only able to simulate the relationship between SSH and chlorophyll in the

516   southern part of the domain? We hypothesize this is due to differences in stratification

517   between the two regions. The average water temperature (colors) and the macronutrient (PO_4)

518   concentrations (contours) for model year 197 are compared to the corresponding measured

519   values in World Ocean Atlas (WOA09) within the upper 200m in the northern (60°-66°E and

520   19°-23°N) and southern (60°-66°E and 15°-17°N) part of the region are shown in Fig. 13. In

521   the northern part of the region (see Fig 13a and b), the GFDL model provides a reasonably

522   good estimation of the mean temperature field near the surface, but subsurface temperatures

523   are not as consistent as there is far too little stratification. This is also associated with a very

524   weak nutricline in CM2.6. Variations in isopycnal depth will therefore not lead to big

525   differences in nutrient supply. Figs. 13c and d show the same fields for the southern part of

526   the region. Unlike the northern part of the domain, the temperature gradient over these depths

527   is well estimated by CM2.6. While the nutricline is still too weak there is some gradient in

528   nutrients between 80 and 120m.

529   As seen in Fig. 1d both the ARGO and WOA09 wintertime mixed layer depth is considerably

17

530 deeper than the summertime mixed layer depth, reaching a maximum of 65m. However, in
531 the northern regions of the model the MLD seems to be too deep in winter, reaching values of
532 130-150 m. This suggests that the overly deep mixed layer in the northern part of the region
533 may explain both the tendency towards an overly strong winter bloom and the failure of
534 mesoscale eddies in modulating chlorophyll blooms. If we look during the time period where
535 we have eddies E1 and E2 (Nov-Dec. year 197, Fig 6c,d) we see shallower mixed layers
536 associated with both eddies.

537 Both the temperature and mixed layer biases in the northern part of the Arabian Sea may
538 result from having too much water from the Persian Gulf in this region. This can be seen in
539 the yearly averaged subsurface salinity-density distribution over the region, shown in Figs 13e
540 and f for both WOA09 data and CM2.6 (model year 197), respectively. Fig. 13e shows two
541 separate tongues of salty water, one near the surface and one at the depth of ~300m. These
542 salty water signals are consistent with the seasonal cycle of Persian Gulf outflow as discussed
543 in Ezam et al. (2010). On the other hand, CM2.6 shows one subsurface salty water signal
544 from the northern part, which is deep and strong enough to result in weak stratification in the
545 north to a depth of 250m, as shown in Fig. 13f. These results suggest that a sharp thermocline
546 and nutricline is necessary for eddy activity to modulate the mixing of nutrients to the surface.

547 We test the idea that a sharper thermocline could modulate mixing of nutrients to the surface
548 by looking at the sources of nutrient in the southern part of Arabian Sea where eddy-bloom
549 relationships similar to observations are occasionally seen. Accordingly, the region containing
550 eddy E1 in Fig. 12 is analyzed to determine the physical mechanisms by which nutrient is
551 transported into the surface layer. Fig. 14 contrasts chlorophyll concentration, advection, and
552 diffusion terms for the region from 63°-66^oE, 15°-18^oN over the December of two consecutive
553 CM2.6 years of 197 and 198. In December of year 197 we see an eddy associated with a
554 bloom while there is no eddy in December of year 198 and the chlorophyll concentrations are
555 much lower. In both years the diffusive flux of nutrient to the top 50m mirrors the
556 chlorophyll. But in 197 it is larger and positive (~10 mol/m^2/month) in the eddy while the
557 advective flux is actually negative in this region. By contrast in Year 198, there is no cyclonic
558 eddy and the diffusive fluxes are much smaller.

559 The bloom associated with eddies E1 and E2 do not fit with any of the mechanisms
560 highlighted in Gaube et al. (2014). We first consider the mechanism of trapping. Eddy E1 is
561 generated in the ocean interior, not as a result of coastal upwelling. As shown in Fig. 15, the

562   nutrient supply rate ranges between 5 and 8 mmol/m^2/month in the eddy. The concentrations

563   in this eddy are only 0.01 µM (5 mmol/m^2) over the top 50 m. It cannot be the case that the

564   nutrients in the eddy can last for several months as a result of "trapping", there must be a

565   continuous supply. Moreover although eddy E2 shows a horizontal advection signal in

566   November (with a positive ring around the edge in Fig. 12a), the signal in December has the

567   opposite sign. Eddy intensification is also an unlikely mechanism for explaining the blooms,

568   as dSSH/dt is relatively small (particularly if we track the minimum SSH associated with E1

569   in Fig. 12c or E2 in Fig. 12d). Finally, Ekman pumping signatures in Gaube et al. (2014) have

570   the opposite sign as what is seen in E1 and E2.

571   Our results also contrast with those in Resplandy et al. (2011). The focus in Resplandy et al.

572   (2011) is on the productivity driven by horizontal and vertical advection in summer and

573   mostly vertical advection in winter. This contradicts our finding of a primary diffusive source

574   of nutrient in winter although it is consistent the finding of advective source of nutrients in

575   summer. We point out that in our model, the only two eddies that actually look like what we

576   see in the satellite observations involve enhanced mixing from below. This is a different result

577   from Levy et al. (2014) and Resplandy et al. (2011). Moreover it is not clear whether these

578   papers get the seasonal correlation with SSH or not. Resplandy et al. (2011) do not focus on

579   structures at the eddy scale as they are more concerned with the net impact of eddies.

580

581   To summarize, we hypothesize that

582   1. The reason that blooms are found in cyclones in the Arabian Sea during the NEM is that

583   the dominant source of nutrients to the surface, i.e. mixing (Barimalala et al., 2013;

584   Kawamiya and Oschlies, 2003) is concentrated there.

585   2. Interannual variability in wintertime blooms in the Northwest Arabian Sea is controlled by

586   the combined presence of these eddies and strength of wintertime cooling.

587   3. Excessive mixing (resulting in too weak a thermocline) prevents mixing from being

588   modulated by eddies in the model except occasionally in the southern part of our region. In

589   the real world the modulation of mixing seen in Fig. 14 extends into the Northwest Arabian

590   Sea and the Gulf of Oman.

591

5 Conclusions

Our analysis of bloom variability in the northwestern Arabian Sea and Gulf of Oman has illustrated both similar and dissimilar descriptive features between satellites and a suite of models and explored the various mechanisms involved. Satellite analyses demonstrate the existence of two blooms, the stronger one associated with the Southwest Monsoon and the weaker one associated with the Northeast Monsoon as also shown by Madhupratap et al. (1996), Kawamiya and Oschlies (2003), Murtugudde et al. (2007), and Al-Azri et al. (2010). We demonstrate a pronounced anti-correlation between SSHA and chlorophyll blooms during certain times in northern winter but a much weaker relationship in other months (typically northern summer) with the relationship disappearing as the blooms vanish in the months of April and May (northern spring). While the depth of thermocline and nutricline and also the stratification affect the convection during the Northeast Monsoon (Dickey et al., 1998; Kumar et al., 2001; Wiggert et al., 2002), we show that a thin nutricline/thermocline and a strong stratification are also required to enable cold eddies to bring nutrients to euphotic zone and develop phytoplankton blooms. During the wintertime monsoon, while both cooling in the winter and eddies control the blooms, variability in bloom location will arise from variability in the location of eddies, and so may not be predictable. In contrast, during the Southwest Monsoon the dominant upwelling associated with the intense environmental forcing supersedes the effect of eddies and the activity of the cold eddies is not pronounced.

Understanding of this phenomenon has been sought using five different 3D ocean-atmosphere models, including a CORE-forced ocean with the TOPAZ biogeochemistry, a coupled model with the TOPAZ biogeochemistry and CM2.6. Because the coarse models with TOPAZ are not able to capture eddies and the interannual variability, CM2.6 (miniBLING), a eddy-resolving high resolution model, was also considered for simulating the spatial and temporal changes of the bloom in the region. This model simulates the two blooms seen in the data and shows that the nutrients driving the northern summer bloom are supplied by advection while those driving the wintertime bloom are supplied by vertical diffusion. However, this model is unable to simulate the seasonal relationship observed in the satellite products between blooms and sea surface height. Although there is some anti-correlation, it tends to be associated with larger spatial scales and not really related to eddies. Instead, eddies in the model usually wrap the chlorophyll around themselves, producing high chlorophyll concentrations around their edges and not at their centers. Comparing the model results to field measurements (WOA09)

624 showed that the model does not account for the strong thermocline and nutricline in the
625 northern part of the region. In the wintertime, this leads to excessive convective supply of
626 nutrients and too strong of a bloom. However, for a few cases, eddies with blooms at the
627 center are tracked in the southern part of the domain. In this region, consistency is observed
628 between the model results and the field data. Analysis of the term balances in mixed layer
629 show that eddies in this region modulate the diffusive supply of nutrients. We suggest that
630 what happens in the model in the Southern Arabian Sea actually describes the Arabian Sea as
631 a whole according to the observations and the field data. The model misses the eddy signal in
632 the north because it lacks a thin nutricline, motions of which will lead to differences in
633 nutrient supply. In the real world, eddies modulate the diffusive supply of nutrients during the
634 wintertime and there is more mixing in the eddy centers along with the diffusive supply
635 provided by the cooling in the wintertime.

636 Accordingly, there is a potential to improve the numerical models by better simulating the
637 Persian Gulf Outflow to produce a sharper thermocline, allowing more realistic nutrient
638 supply. Overflows are difficult to simulate in level-coordinate models because they are prone
639 to excessive entrainment of the dense plume (Winton et al., 1998). While significant effort
640 has gone into simulating the Denmark Straits overflow at coarse resolution (Legg et al.,
641 2009), our results show that smaller overflows such as the Persian Gulf may be regionally
642 significant. This may provide further impetus for using isopycnal models in high resolution
643 simulations, as such models can potentially simulate such overflows with greater fidelity.

644 It is worth noting that regional models, (such as Resplandy et al. (2011)) do have the potential
645 to better simulate the hydrography of the Northern Arabian Sea. Because such models are
646 very tightly constrained through "sponges" that restore hydrography at the boundaries, they
647 may not have the problems that global models do at representing the effects of overflows that
648 they do not properly simulate. However, such models cannot by themselves simulate the
649 effects of changing climate, which in turn changes the boundary conditions. For this reason,
650 global models must still be used for projection, making it important to identify the reasons
651 that they are not going to work.

652

653

654

664   **References**

665   Adcroft, A., Campin, J.-M., Hill, C. and Marshall, J.: Implementation of an Atmosphere–
666   Ocean General Circulation Model on the Expanded Spherical Cube, Mon. Weather Rev.,
667   132(12), 2845–2863, doi:10.1175/MWR2823.1, 2004.

668   Al-Azri, A. R., Piontkovski, S. A., Al-Hashmi, K. A., Goes, J. I., Gomes, H. D. R. and
669   Glibert, P. M.: Mesoscale and Nutrient Conditions Associated with the Massive 2008
670   Cochlodinium polykrikoides Bloom in the Sea of Oman/Arabian Gulf, Estuaries and Coasts,
671   doi:10.1007/s12237-013-9693-1, 2013.

672   Al-Azri, A. R., Piontkovski, S. A., Al-Hashmi, K. A., Goes, J. I. and Gomes, H. R.:
673   Chlorophyll a as a measure of seasonal coupling between phytoplankton and the monsoon
674   periods in the Gulf of Oman, Aquat. Ecol., 44(2), 449–461, doi:10.1007/s10452-009-9303-2,
675   2010.

676   Anderson, D. M. and Prell, W. L.: A 300 KYR Record of Upwelling Off Oman During the
677   Late Quaternary: Evidence of the Asian Southwest Mansoon, Paleoceanography, 8(2), 193–
678   208, 1993.

679   ARGO: Climatology, [online] Available from: http://www.argo.ucsd.edu, 2015.

680   Armstrong, R. A., Lee, C., Hedges, J. I., Honjo, S. and Wakeham, S. G.: A new, mechanistic
681   model for organic carbon fluxes in the ocean based on the quantitative association of POC
682   with ballast minerals, Deep. Res. Part II Top. Stud. Oceanogr., 49(1-3), 219–236,
683   doi:10.1016/S0967-0645(01)00101-1, 2002.

684   Banse, K. and McClain, C. R.: Winter blooms of phytoplankton in the Arabian Sea as
685   observed by the Coastal Zone Color Scanner, Mar Ecol Prog Ser, 34, 201–211, 1986.

686   Barimalala, R., Bracco, A., Kucharski, F., McCreary, J. P. and Crise, A.: Arabian Sea
687   ecosystem responses to the South Tropical Atlantic teleconnection, J. Mar. Syst., 117-118,
688   14–30, doi:10.1016/j.jmarsys.2013.03.002, 2013.

689   Bartolacci, D. M. and Luther, M. E.: Patterns of co-variability between physical and
690   biological parameters in the Arabian Sea, Deep Sea Res. Part II Top. Stud. Oceanogr., 46(8-
691   9), 1933–1964, doi:10.1016/S0967-0645(99)00049-1, 1999.

692   Behrenfeld, M. J.: Abandoning Sverdrup's Critical Depth Hypothesis on phytoplankton
693   blooms, Ecology, 91(4), 977–989, doi:10.1890/09-1207.1, 2010.

694   Behrenfeld, M. J., Boss, E., Siegel, D. A. and Shea, D. M.: Carbon-based ocean productivity
695   and phytoplankton physiology from space, Global Biogeochem. Cycles, 19(1), 1–14,
696   doi:10.1029/2004GB002299, 2005.

697   Bryan, K. and Lewis, L. J.: A Water Mass Moel of the World Ocean, 84(8), 2503, 1979.

698   Danabasoglu, G., Large, W. G., Tribbia, J. J., Gent, P. R., Briegleb, B. P. and McWilliams, J.
699   C.: Diurnal coupling in the tropical oceans of CCSM3, J. Clim., 19(11), 2347–2365,
700   doi:10.1175/JCLI3739.1, 2006.

701   Delworth, T. L., Broccoli, A. J., Rosati, A., Stouffer, R. J., Balaji, V., Beesley, J. A., Cooke,
702   W. F., Dixon, K. W., Dunne, J., Dunne, K. A., Durachta, J. W., Findell, K. L., Ginoux, P.,
703   Gnanadesikan, A., Gordon, C. T., Griffies, S. M., Gudgel, R., Harrison, M. J., Held, I. M.,
704   Hemler, R. S., Horowitz, L. W., Klein, S. A., Knutson, T. R., Kushner, P. J., Langenhorst, A.
705   R., Lee, H. C., Lin, S. J., Lu, J., Malyshev, S. L., Milly, P. C. D., Ramaswamy, V., Russell, J.,

706 Schwarzkopf, M. D., Shevliakova, E., Sirutis, J. J., Spelman, M. J., Stern, W. F., Winton, M.,
707 Wittenberg, A. T., Wyman, B., Zeng, F. and Zhang, R.: GFDL's CM2 global coupled climate
708 models. Part I: Formulation and simulation characteristics, J. Clim., 19(5), 643–674,
709 doi:10.1175/JCLI3629.1, 2006.

710 Delworth, T. L., Rosati, A., Anderson, W., Adcroft, A. J., Balaji, V., Benson, R., Dixon, K.,
711 Griffies, S. M., Lee, H.-C., Pacanowski, R. C., Vecchi, G. A., Wittenberg, A. T., Zeng, F. and
712 Zhang, R.: Simulated Climate and Climate Change in the GFDL CM2.5 High-Resolution
713 Coupled Climate Model, J. Clim., 25(8), 2755–2781, doi:10.1175/JCLI-D-11-00316.1, 2012.

714 Dickey, T., Marra, J., Sigurdson, D. E., Weller, R. A., Kinkade, C. S., Zedler, S. E., Wiggert,
715 J. D. and Langdon, C.: Seasonal variability of bio-optical and physical properties in the
716 Arabian Sea : October 1994 — October 1995, Deep. Res. II, 45(October 1994), 2001–2025,
717 1998.

718 Dunne, J., Gnanadesikan, A., Sarmiento, J. L. and Slater, R. D.: Technical description of the
719 prototype version (v0) of Tracers Of Phytoplankton with Allometric Zooplankton (TOPAZ)
720 ocean biogeochemical model as used in the Princeton IFMIP* model, Biogeosciences Suppl.,
721 7(1), 3593, doi:10.5194/bg-7-3593-2010, 2010.

722 Dunne, J. P., John, J. G., Adcroft, A. J., Griffies, S. M. and Hallberg, R. W.: GFDL's ESM2
723 Global Coupled Climate-Carbon Earth System Models. Part I: Physical Formulation and
724 Baseline Simulation Characteristics, J. Clim., 25, 6646–6665,
725 doi:http://dx.doi.org/10.1175/JCLI-D-11-00560.1, 2012.

726 Dunne, J. P., John, J. G., Shevliakova, S., Stouffer, R. J., Krasting, J. P., Malyshev, S. L.,
727 Milly, P. C. D., Sentman, L. T., Adcroft, A. J., Cooke, W., Dunne, K. A., Griffies, S. M.,
728 Hallberg, R. W., Harrison, M. J., Levy, H., Wittenberg, A. T., Phillips, P. J. and Zadeh, N.:
729 GFDL's ESM2 global coupled climate-carbon earth system models. Part II: Carbon system
730 formulation and baseline simulation characteristics, J. Clim., 26(7), 2247–2267,
731 doi:10.1175/JCLI-D-12-00150.1, 2013.

732 Dunne, J. P., Sarmiento, J. L. and Gnanadesikan, A.: A synthesis of global particle export
733 from the surface ocean and cycling through the ocean interior and on the seafloor, Global
734 Biogeochem. Cycles, 21(4), 1–16, doi:10.1029/2006GB002907, 2007.

735 Ezam, M., Bidokhti, A. A. and Javid, A H.: Numerical simulations of spreading of the Persian
736 Gulf outflow into the Oman Sea, Ocean Sci., 6(4), 887–900, doi:10.5194/os-6-887-2010,
737 2010.

738 Fischer, A. S., Weller, R. A., Rudnick, D. L., Eriksen, C. C., Lee, C. M., Brink, K. H., Fox, C.
739 A. and Leben, R. R.: Mesoscale eddies, coastal upwelling, and the upper-ocean heat budget in
740 the Arabian Sea, Deep Sea Res. Part II Top. Stud. Oceanogr., 49(12), 2231–2264,
741 doi:10.1016/S0967-0645(02)00036-X, 2002.

742 Fox-Kemper, B., Ferrari, R. and Hallberg, R.: Parameterization of Mixed Layer Eddies. Part
743 I: Theory and Diagnosis, J. Phys. Oceanogr., 38(6), 1145–1165, doi:10.1175/2007JPO3792.1,
744 2008.

745 Galbraith, E. D., Dunne, J. P., Gnanadesikan, A., Slater, R. D., Sarmiento, J. L., Dufour, C.
746 O., de Souza, G. F., Bianchi, D., Claret, M., Rodgers, K. B. and Sedigh Marvasti, S.:
747 Complex functionality with minimal computation: Promise and pitfalls of reduced-tracer
748 ocean biogeochemistry models, J. Adv. Model. Earth Syst., 1–17,
749 doi:10.1002/2015MS000463, 2015.

750 Gaube, P., McGillicuddy, D., Chelton, D., Behrenfeld, M. J. and Strutton, P.: Regional
751 variations in the influence ofmesoscale eddies on near-surface chlorophyll Peter, J. Geophys.
752 Res. Ocean., 119, 8195–8220, doi:10.1002/2014JC010111.Received, 2014.

753 Gnanadesikan, A., Dixon, K. W., Griffies, S. M., Balaji, V., Barreiro, M., Beesley, J. A.,
754 Cooke, W. F., Delworth, T. L., Gerdes, R., Harrison, M. J., Held, I. M., Hurlin, W. J., Lee, H.
755 C., Liang, Z., Nong, G., Pacanowski, R. C., Rosati, A., Russell, J., Samuels, B. L., Song, Q.,
756 Spelman, M. J., Stouffer, R. J., Sweeney, C. O., Vecchi, G., Winton, M., Wittenberg, A. T.,
757 Zeng, F., Zhang, R. and Dunne, J. P.: GFDL's CM2 global coupled climate models. Part II:
758 The baseline ocean simulation, J. Clim., 19(5), 675–697, doi:10.1175/JCLI3630.1, 2006.

759 Gnanadesikan, A., Dunne, J. P. and John, J.: What ocean biogeochemical models can tell us
760 about bottom-up control of ecosystem variability, ICES J. Mar. Sci., 68(6), 1030–1044,
761 doi:10.1093/icesjms/fsr068, 2011.

762 Gnanadesikan, A., Dunne, J. P. and Msadek, R.: Connecting Atlantic temperature variability
763 and biological cycling in two earth system models, J. Mar. Syst., 133, 39–54,
764 doi:10.1016/j.jmarsys.2013.10.003, 2014.

765 Goes, J. I., Thoppil, P. G., Gomes, H. D. R. and Fasullo, J. T.: Warming of the Eurasian
766 landmass is making the Arabian Sea more productive., Science, 308(5721), 545–547,
767 doi:10.1126/science.1106610, 2005.

768 Gomes, R., Goes, J. I., Matondkar, S. G. P., Parab, S. G., Al-azri, A. R. N. and Thoppil, P. G.:
769 Deep-Sea Research I Blooms of Noctiluca miliaris in the Arabian Sea — An in situ and
770 satellite study, Deep Sea Res. Part I Oceanogr. Res. Pap., 55, 751–765,
771 doi:10.1016/j.dsr.2008.03.003, 2008.

772 Griffies, S. M., Biastoch, A., Böning, C., Bryan, F., Danabasoglu, G., Chassignet, E. P.,
773 England, M. H., Gerdes, R., Haak, H., Hallberg, R. W., Hazeleger, W., Jungclaus, J., Large,
774 W. G., Madec, G., Pirani, A., Samuels, B. L., Scheinert, M., Gupta, A. Sen, Severijns, C. A.,
775 Simmons, H. L., Treguier, A. M., Winton, M., Yeager, S. and Yin, J.: Coordinated Ocean-ice
776 Reference   Experiments   (COREs),   Ocean   Model.,   26(1-2),   1–46,
777 doi:10.1016/j.ocemod.2008.08.007, 2009.

778 Griffies, S. M., Gnanadesikan, A., Dixon, K. W., Dunne, J. P., Gerdes, R., Harrison, M. J.,
779 Rosati, A., Russell, J. L., Samuels, B. L., Spelman, M. J., Winton, M. and Zhang, R.:
780 Formulation of an ocean model for global climate simulations, Ocean Sci. Discuss., 2(3),
781 165–246, doi:10.5194/osd-2-165-2005, 2005.

782 Hamzehei, S. and Bidokhti, A.: Red tide monitoring in the Persian Gulf and Gulf of Oman
783 using MODIS sensor data., Tech. J. …, 1100–1107, 2013.

784 Honjo, S., Dymond, J., Prell, W. and Ittekkot, V.: Monsoon-controlled export fluxes to the
785 interior of the Arabian Sea, Deep. Res. II, 46(1999), 1859–1902, 2000.

786 Kawamiya, M. and Oschlies, A.: An eddy-permitting , coupled ecosystem-circulation model
787 of the Arabian Sea : comparison with observations, J. Mar. Syst., 38, 221–257, 2003.

788 Klaas, C. and Archer, D. E.: Association of sinking organic matter with various types of
789 mineral ballast in the deep sea: Implications for the rain ratio, Global Biogeochem. Cycles,
790 16(4), 1116, doi:10.1029/2001GB001765, 2002.

791 Kostadinov, T. S., Siegel, D. A. and Maritorena, S.: Retrieval of the particle size distribution
792 from satellite ocean color observations, J. Geophys. Res., 114(C9), C09015,

793   doi:10.1029/2009JC005303, 2009.

794   Kumar, S. P., Ramaiah, N., Gauns, M., Sarma, V. V. S. S., Muraleedharan, P. M.,
795   Raghukumar, S., Kumar, M. D. and Madhupratap, M.: Physical forcing of biological
796   productivity in the Northern Arabian Sea during the Northeast Monsoon, Deep. Res. II, 48,
797   1115–1126, 2001.

798   Large, W. G., McWilliams, J. C. and Doney, S. C.: Oceanic vertical mixing: A review and a
799   model with a nonlocal boundary layer parameterization, Rev. Geophys., 32(4), 363,
800   doi:10.1029/94RG01872, 1994.

801   Legg, S., Briegleb, B., Chang, Y., Chassignet, E. P., Danabasoglu, G., Ezer, T., Gordon, A.
802   L., Griffies, S., Hallberg, R., Jackson, L., Large, W., Özgükmen, T. M., Peters, H., Price, J.,
803   Riemenschneider, U., Wu, W., Xu, X. and Yang, J.: Improving oceanic overflow
804   representation in climate models: The Gravity Current Entrainment Climate Process Team,
805   Bull. Am. Meteorol. Soc., 90(5), 657–670, doi:10.1175/2008BAMS2667.1, 2009.

806   Levy, M., Resplandy, L. and Lengaigne, M.: Oceanicmesoscale turbulence drives large
807   biogeochemical interannual variability atmiddle and high latitudes, Geophys. Res. Lett.,
808   41(7), 2467–2474, doi:10.1002/2014GL059608, 2014.

809   Levy, M., Shankar, D., Andre, J., Shenoi, S. S. C., Durand, F. and Montegut, C. D. B.: Basin-
810   wide seasonal evolution of the Indian Ocean ' s phytoplankton blooms, J. Geophys. Res.,
811   112(C12014), 1–14, 2007.

812   Madhupratap, M., Kumar, S., Bhattathiri, P., Kumar, M., Raghukumar, S., Nair, K. and
813   Ramaiah, N.: Mechanism of the biological response to winter cooling in the northeastern
814   Arabian Sea, Nature, 384(12), 549–552, 1996.

815   Maritorena, S., Siegel, D. and Peterson, A. R.: Optimization of a semianalytical ocean color
816   model for global-scale applications., Appl. Opt., 41(15), 2705–14, 2002.

817   McGillicuddy, D., Kosnyrev, V., Ryan, J. and Yoder, J.: Covariation of mesoscale ocean
818   color and sea-surface temperature patterns in the Sargasso Sea, Deep. Res. II, 48, 1823–1836,
819   2001.

820   Murtugudde, R., Seager, R. and Thoppil, P.: Arabian Sea response to monsoon variations,
821   Paleoceanography, 22(4), 1–17, doi:10.1029/2007PA001467, 2007.

822   Naqvi, S. W. A., Moffett, J. W., Gauns, M. U., Narvekar, P. V, Pratihary, A. K., Naik, H.,
823   Shenoy, D. M., Jayakumar, D. A., Goepfer, T. J., Patra, P. K., Al-Azri, A. and Ahmed, S. I.:
824   The Arabian Sea as a high-nutrient , low-chlorophyll region during the late Southwest
825   Monsoon, Biogeosciences, 7, 2091–2100, doi:10.5194/bg-7-2091-2010, 2010.

826   Piontkovski, S., Al-Azri, A. and Al-Hashmi, K.: Seasonal and interannual variability of
827   chlorophyll-a in the Gulf of Oman compared to the open Arabian Sea regions, Int. J. Remote
828   Sens., 32(22), 7703–7715, doi:10.1080/01431161.2010.527393, 2011.

829   Piontkovski, S., Al-Gheilani, H., Jupp, B., Al-Azri, A. and Al-hashmi, K.: Interannual
830   Changes in the Sea of Oman Ecosystem., Open Mar. Biol. J., 6, 38–52, 2012.

831   Resplandy, L., Lévy, M., Madec, G., Pous, S., Aumont, O. and Kumar, D.: Contribution of
832   mesoscale processes to nutrient budgets in the Arabian Sea, J. Geophys. Res. Ocean., 116(11),
833   1–24, doi:10.1029/2011JC007006, 2011.

834   Richlen, M. L., Morton, S. L., Jamali, E. A., Rajan, A. and Anderson, D. M.: The catastrophic

835 2008–2009 red tide in the Arabian gulf region, with observations on the identification and
836 phylogeny of the fish-killing dinoflagellate Cochlodinium polykrikoides, Harmful Algae,
837 9(2), 163–172, doi:10.1016/j.hal.2009.08.013, 2010.

838 Sarma, Y. V. B., Al-hashmi, K. and Smith, L. S.: Sea Surface Warming and its Implications
839 for Harmful Algal Blooms off Oman, Int. J. Mar. Sci., 3(8), 65–71,
840 doi:10.5376/ijms.2013.03.0008, 2013.

841 Shalapyonok, A., Olson, R. J. and Shalapyonok, L. S.: Arabian Sea phytoplankton during
842 Southwest and Northeast Monsoons 1995 : composition , size structure and biomass from
843 individual cell properties measured by # ow cytometry, Deep. Res. II, 48, 1231–1261, 2001.

844 Simmons, H. L., Jayne, S. R., St. Laurent, L. C. and Weaver, A. J.: Tidally driven mixing in a
845 numerical model of the ocean general circulation, Ocean Model., 6(3-4), 245–263,
846 doi:10.1016/S1463-5003(03)00011-8, 2004.

847 Stacey, M. W., Pond, S. and Nowak, Z. P.: A Numerical Model of the Circulation in Knight
848 Inlet, British Columbia, Canada, J. Phys. Oceanogr., 25(6), 1037–1062, doi:10.1175/1520-
849 0485(1995)025<1037:ANMOTC>2.0.CO;2, 1995.

850 Tang, D., Kawamura, H. and Luis, A. J.: Short-term variability of phytoplankton blooms
851 associated with a cold eddy in the northwestern Arabian Sea, Remote Sens. Environ., 81, 82–
852 89, 2002.

853 Veldhuis, M. J. W., Kraay, G. W., Van Bleijswijk, J. D. L. and Baars, M. A.: Seasonal and
854 spatial variability in phytoplankton biomass , productivity and growth in the northwestern
855 Indian Ocean : the southwest and northeast monsoon , 1992-1993, Deep Sea Res. Part I,
856 44(3), 425–449, 1997.

857 Wang, D. and Zhao, H.: Estimation of phytoplankton responses to Hurricane Gonu over the
858 Arabian Sea based on ocean color data, Sensors, 4878–4893, doi:10.3390/s8084878, 2008.

859 Wiggert, J. D., Murtugudde, R. G. and Christian, J. R.: Annual ecosystem variability in the
860 tropical Indian Ocean : Results of a coupled bio-physical ocean general circulation model,
861 Deep. Res. II, 53, 644–676, doi:10.1016/j.dsr2.2006.01.027, 2006.

862 Wiggert, J. D., Murtugudde, R. G. and Mcclain, C. R.: Processes controlling interannual
863 variations in wintertime (Northeast Monsoon) primary productivity in the central Arabian
864 Sea, Deep. Res. II, 49, 2319–2343, 2002.

865 Winton, M., Hallberg, R. and Gnanadesikan, A.: Simulation of Density-Driven Frictional
866 Downslope Flow in Z -Coordinate Ocean Models, J. Phys. Oceanogr., 28(11), 2163–2174,
867 doi:10.1175/1520-0485(1998)028<2163:SODDFD>2.0.CO;2, 1998.

868
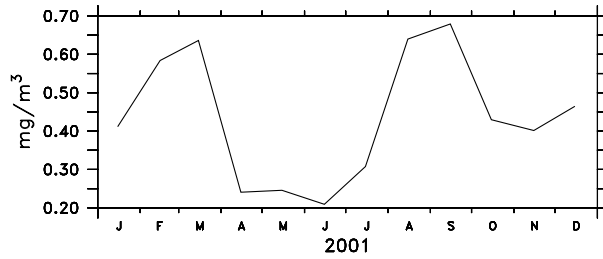
(A) GSM Chlorophyll a (mg/m³)
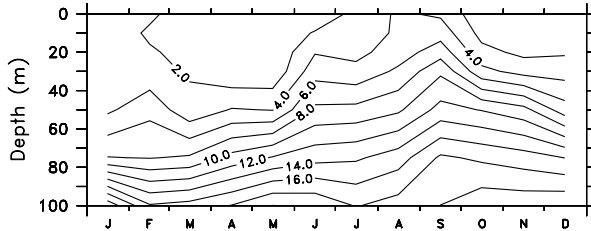
(B) WOA09: Nitrate (micromoles/l)
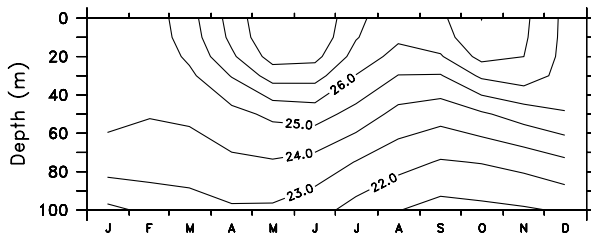
(C) WOA09: Water Temperature (degrees C)
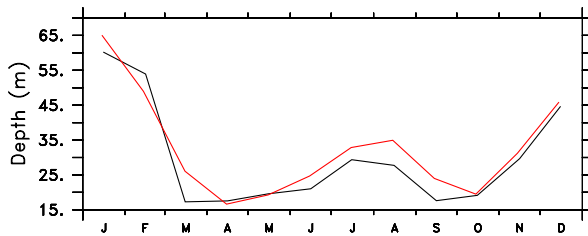
(D) MLD—WOA(Black) , MLD—Argo(Red)

869

870   Figure 1. Monthly average for region from 56°E-66°E, 15°N-26°N: (a) Climatological surface

871   chlorophyll-a (SeaWIFS) for a nominal year of 2001; (b) Nitrate (WOA09) over top 100m;

872   (c) Temperature over top 100m; (d) WOA09 seasonal mixed layer depth in meters- black line

873   shows result from World Ocean Atlas, red line from ARGO climatology (ARGO, 2015).

874
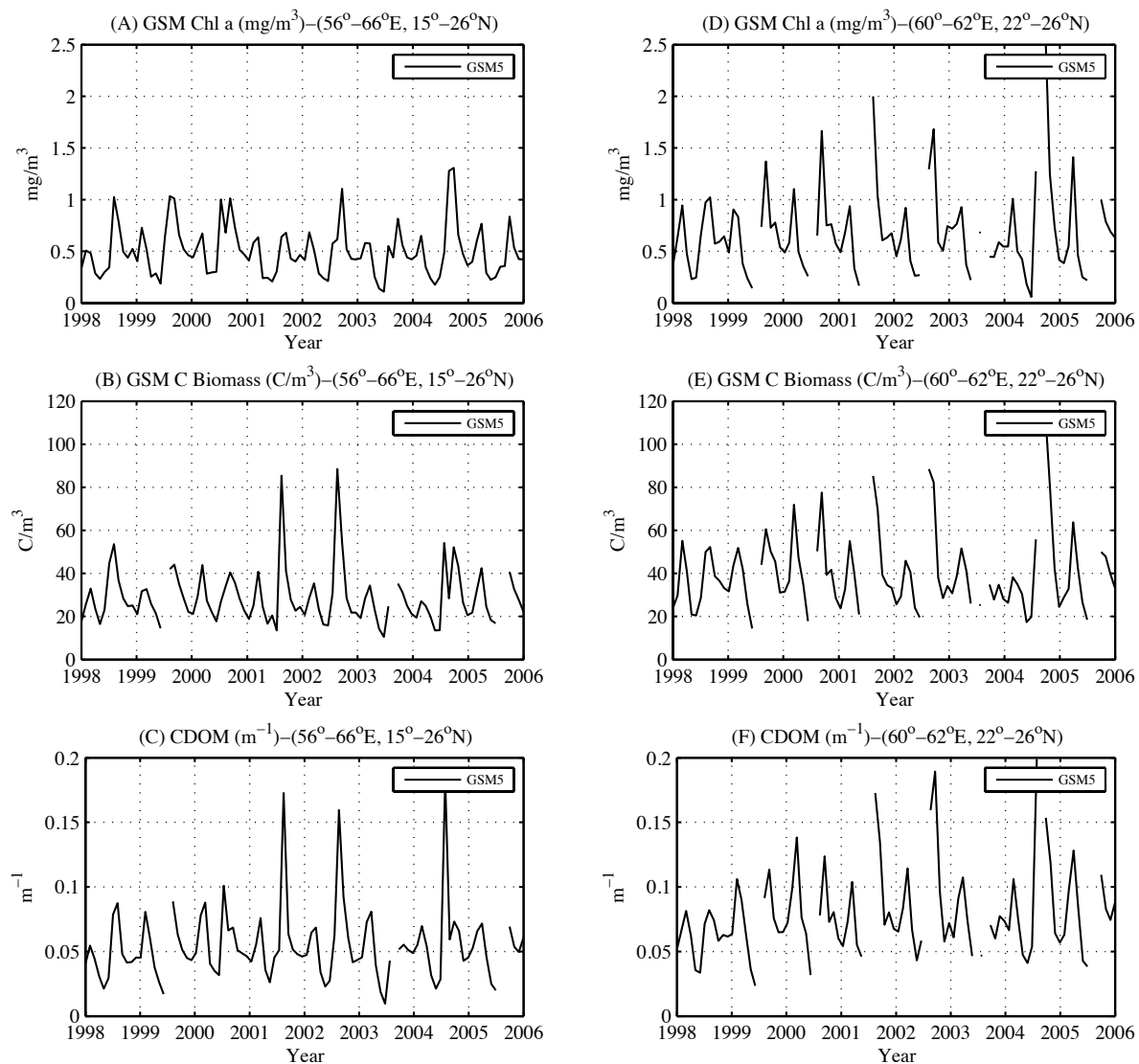
Figure 2. Monthly variation of organic matter in SeaWiFS satellite data between 1998 and 2005 within 56°-66°E, 15°-26°N (large region); and 60°-62°E, 22°-26°N (small region): (a) and (d) chlorophyll; (b) and (e) particulate backscatter; (c) and (f) CDOM.
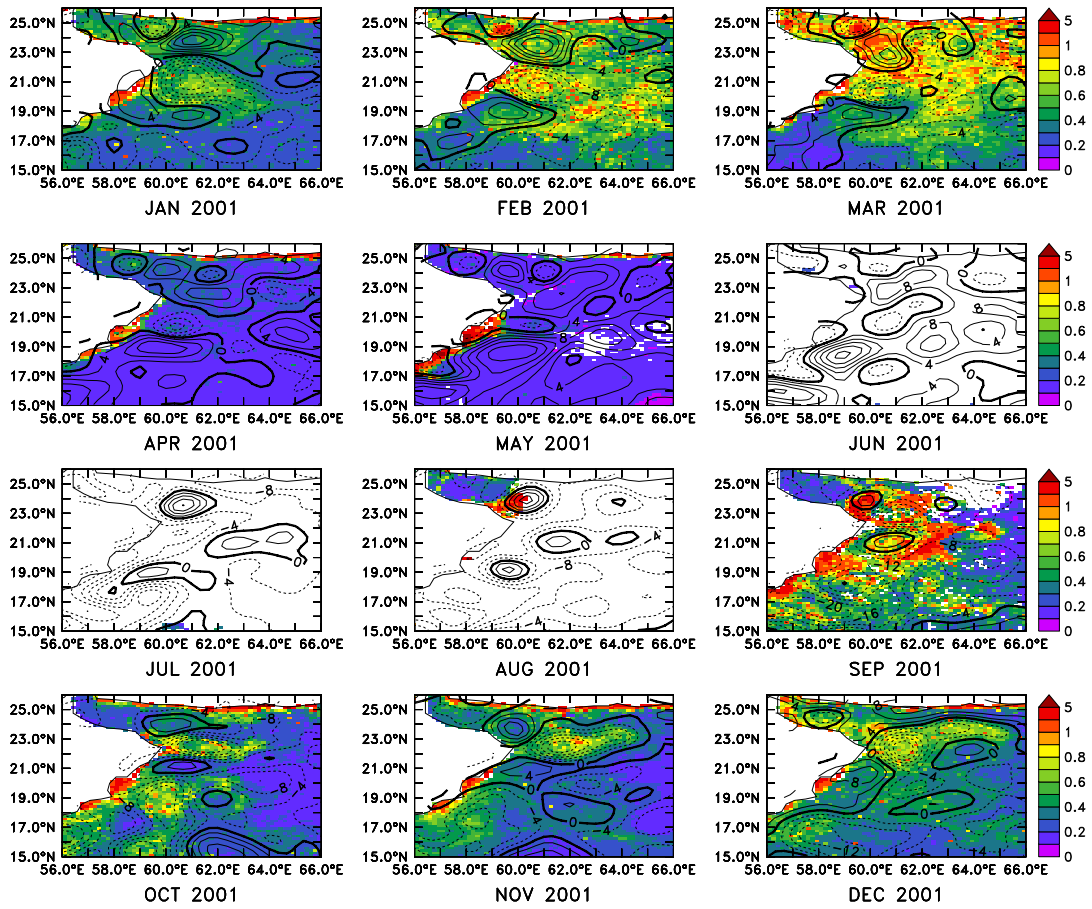
879

880 Figure 3. Satellite chlorophyll-a in mg/m^3 (colors) and sea-surface height anomaly (SSHA,

881 contours) in cm (contour interval = 5cm) in the Gulf of Oman and Northwest Arabian Sea

882 over the course of 2001.

883

884
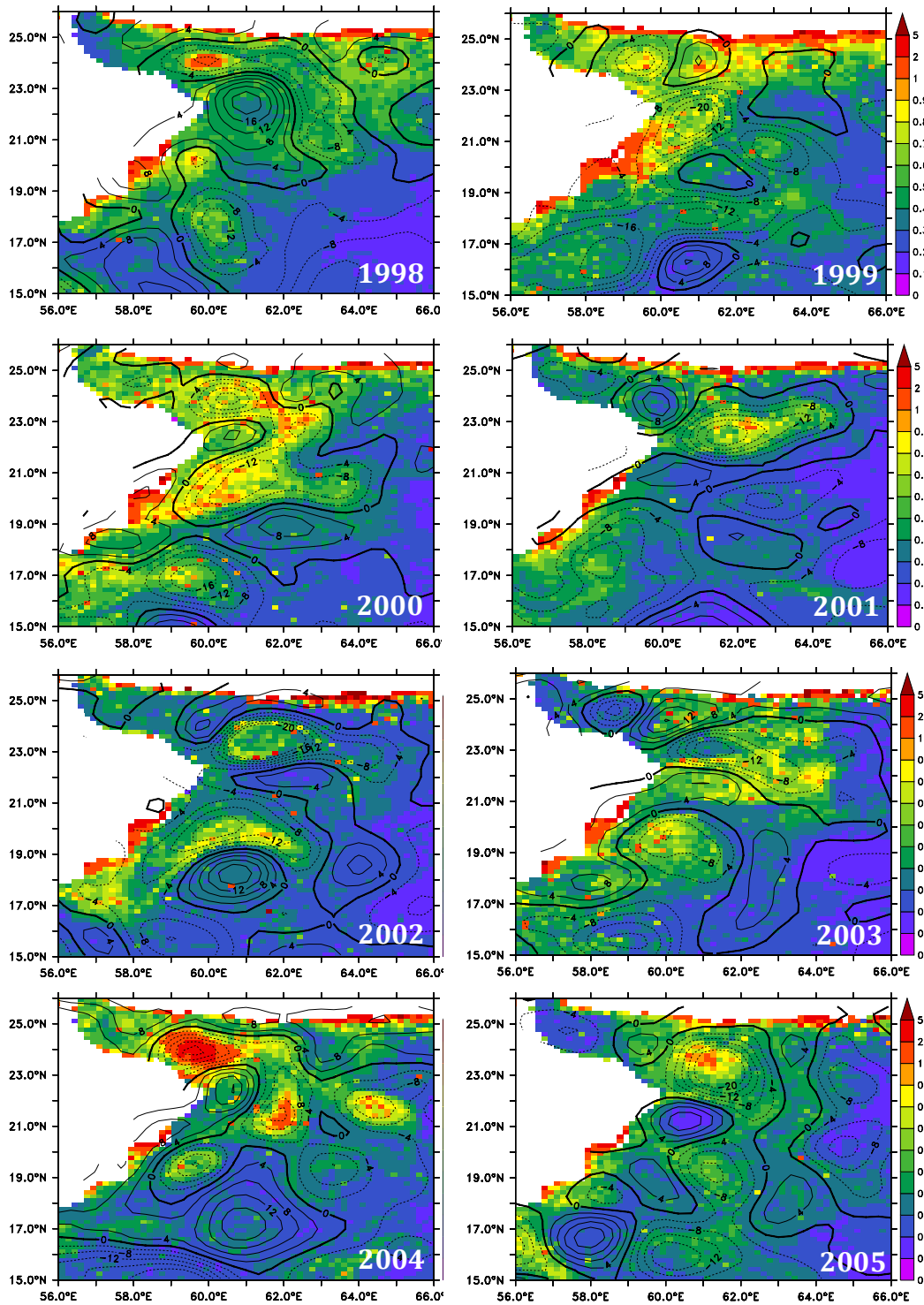
Figure 4. Chlorophyll-a in mgm^{-3} (colors) and sea surface height anomaly (SSHA, contours) in cm (contour interval=5 cm) in the Gulf of Oman and Northwest Arabian Sea during November in different years.

888
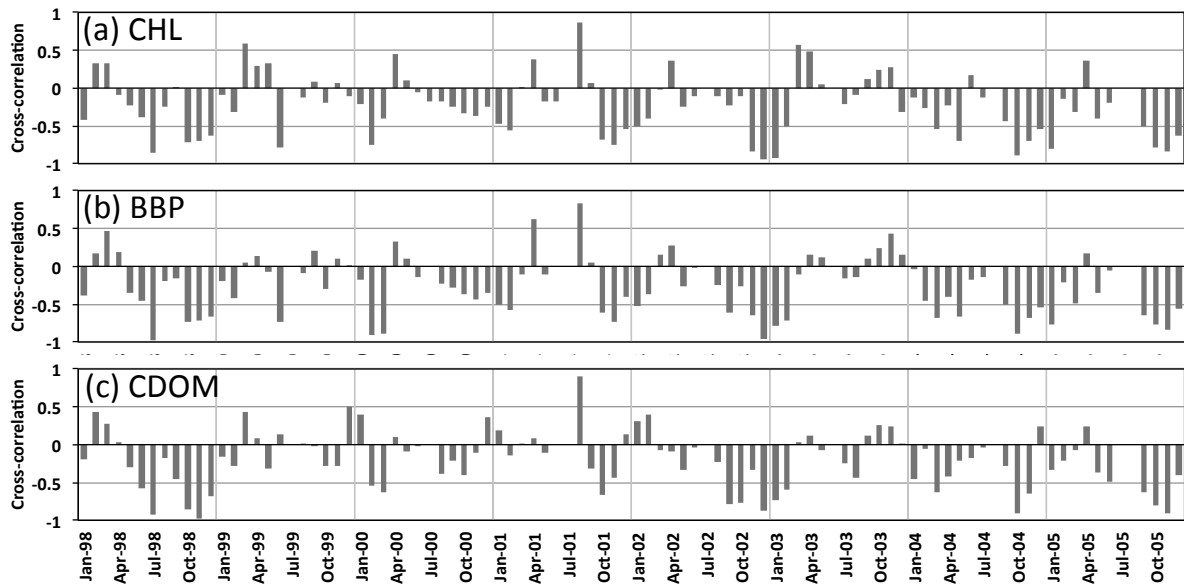
889

890 Figure 5. Monthly cross-correlation with AVISO SSHA between 1998 and 2005 within 56°-
891 66°E and 15°-26°N. for (a) satellite-estimated chlorophyll; (b) satellite estimated BBP; (c)
892 satellite-estimated CDOM.

893
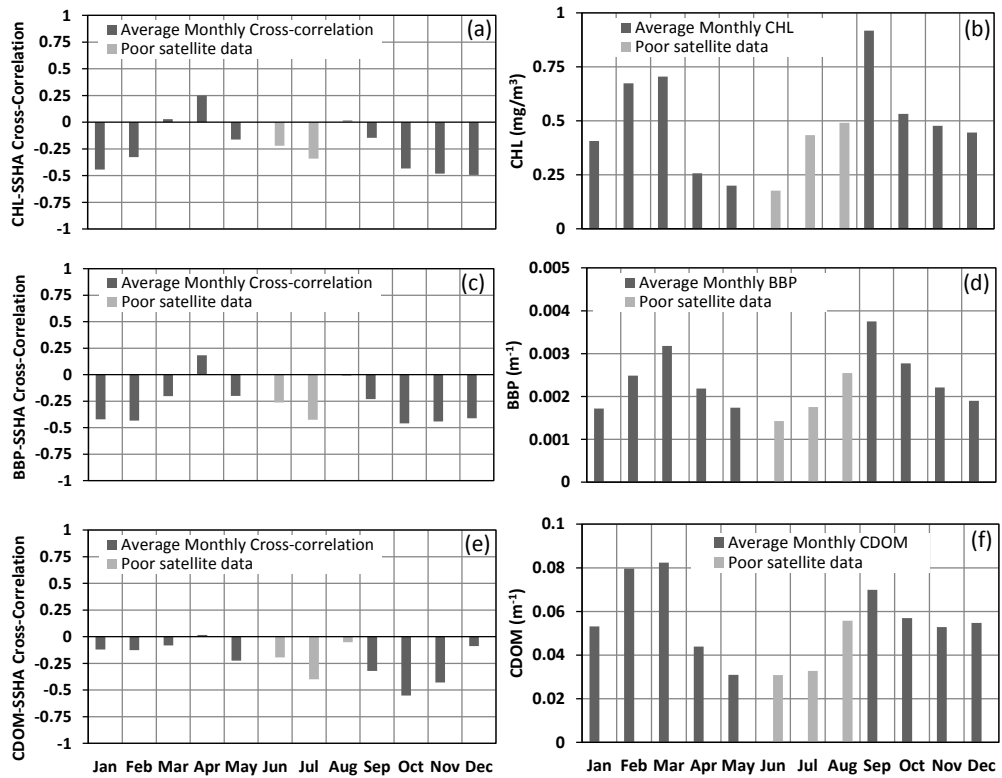
894

895 Figure 6. Average monthly cross-correlation with observed SSHA and average monthly
896 values between 1998 and 2005 within 56°-66°E and 15°-26°N for (a, b) satellite-estimated
897 chlorophyll; (c, d) satellite-estimated backscatter; (e, f) satellite-estimated CDOM.

898

899
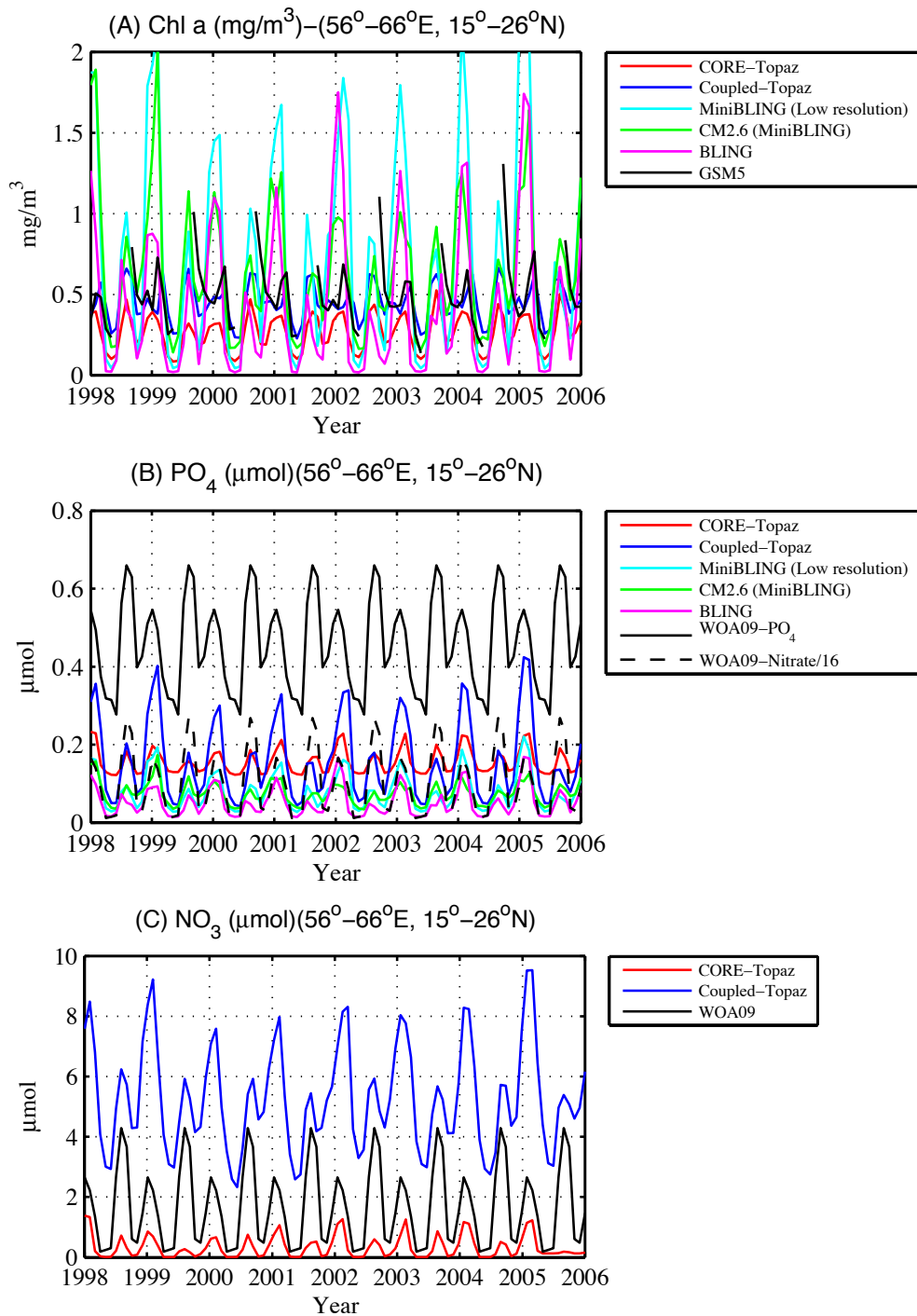
Figure 7. Monthly variation of organic matter in satellite data between 1998 and 2005 and GFDL models (8 characteristic years) within 56°–66°E, 15°–26°N: (a) chlorophyll from GFDL models and GSM5 algorithm. (b) PO_4 from the BLING and miniBLING simulations, $NO_3/16$ from the TOPAZ simulations and observed PO_4 from WOA09. (c) NO_3 from the TOPAZ simulations and observed NO_3 fromWOA09.

905

(a) Mixed Layer Light (W m^{-2})

(b) C–Specific light–saturated photosynthesis rate (S^{-1})
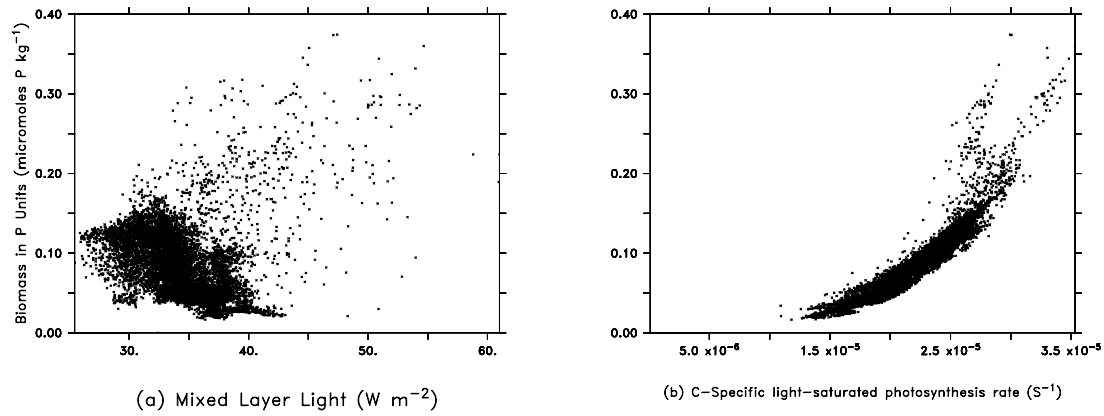
906

907   Figure 8. Modeled biomass in CM2.6 in P units (mol P kg $^{-1}$) versus: (a) Mixed layer

908   irradiance (Wm^{-2}); (b) Light-Saturated photosynthesis rate (carbon specific) (s^{-1}) 56°-66°E,

909   15°-26°N for January of year 195. In the model, biomass is a function of the growth rate

910   smoothed over several days, and the light-saturated photosynthesis rate indicates the extent to

911   which this growth rate is controlled by nutrient limitation.

912
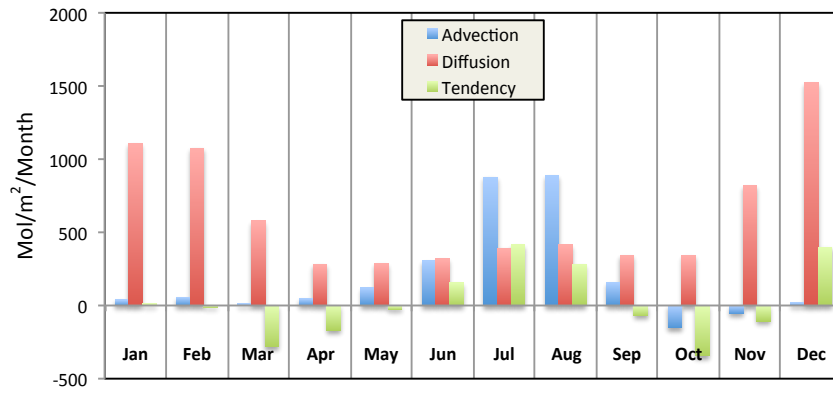
913

914   Figure 9. PO$_4$ Advection, diffusion and tendency flux from the CM2.6 model over the whole

915   region averaged over top 50 m (56°-66°E, 15°-26°N).

916

917

Chl$_a$ C.o.V

0.8

0.6

0.4

0.2

0

Jan   Apr   Jul   Oct

Month

CORE–Topaz
Coupled–Topaz
CM2.6 (miniBLING)
CM2.6 (miniBLING)–South
GSM5
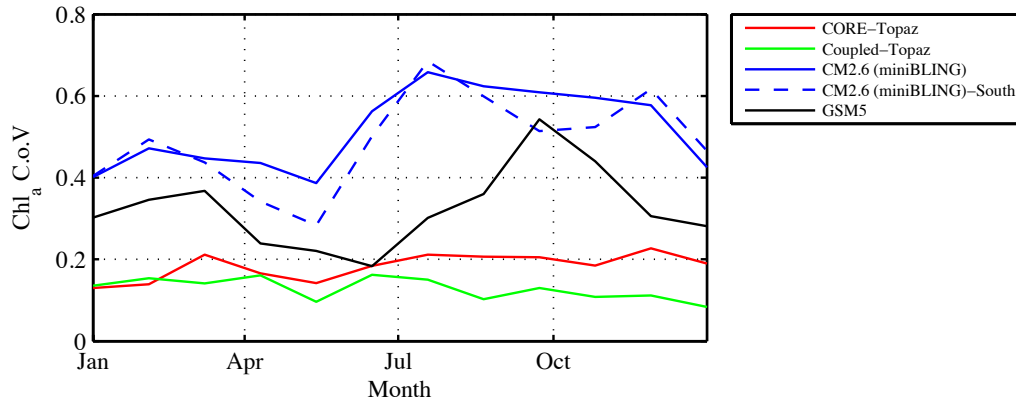
918

919 Figure 10. Average monthly coefficient of variation (standard deviation/mean) of Chlorophyll

920 a in satellite data between 1998 and 2005 and GFDL models (eight characteristics years)

921 within (56°–66^oE, 15°–26^oN) for the satellite data (black), CORE-TOPAZ (red), COUPLED-

922 TOPAZ (green) and CM2.6 model with miniBLING (blue) and within the south region (56°–

923 66^oE, 15°–19^oN) for CM2.6 (miniBLING, dashed blue).

924

925

926
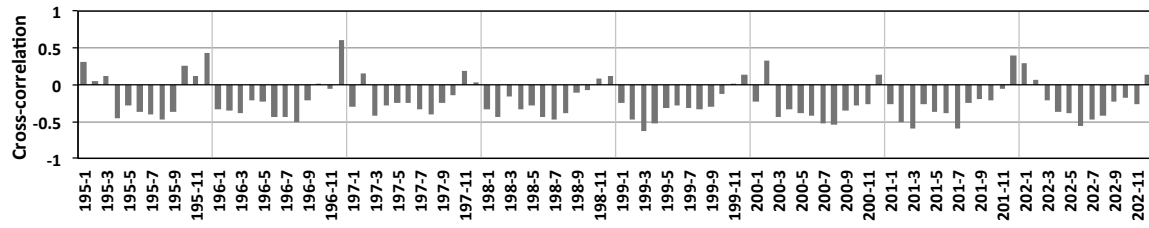
Figure 11. CM2.6 monthly Chlorophyll-SSHA cross-correlation over 8 years within 56°-66°E

and 15°-26°N.
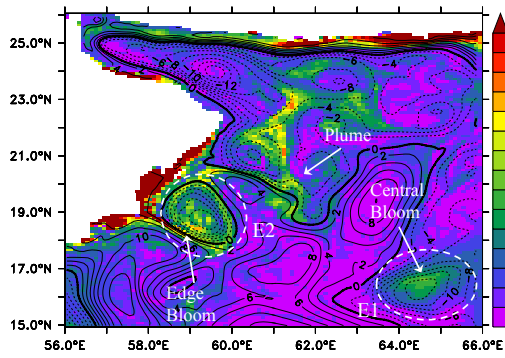
(a) Chlorophyll-a and SSHA at November 9th
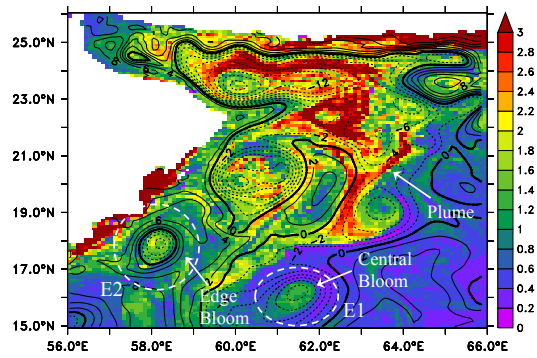
(b) Chlorophyll-a and SSHA at December 28th
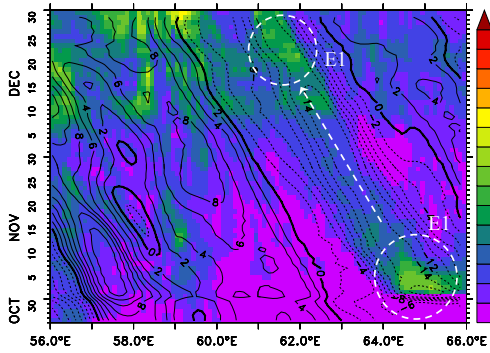
(c) Chlorophyll-a and SSHA: November and December along 16°N
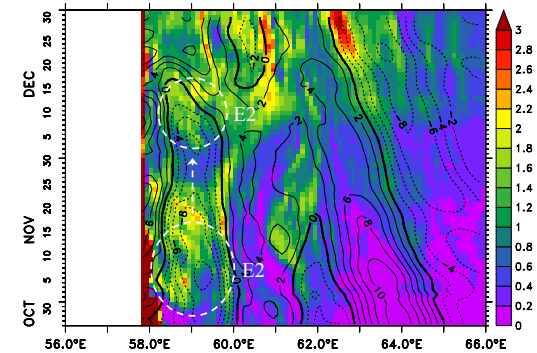
(d) Chlorophyll-a and SSHA: November and December along 19°N

Figure 12. CM2.6 (miniBLING) Surface chlorophyll-a concentration and sea surface height anomaly (SSHA) November and December during a year where the observed eddy-bloom interaction is seen in the Southern part of the Arabian Sea.
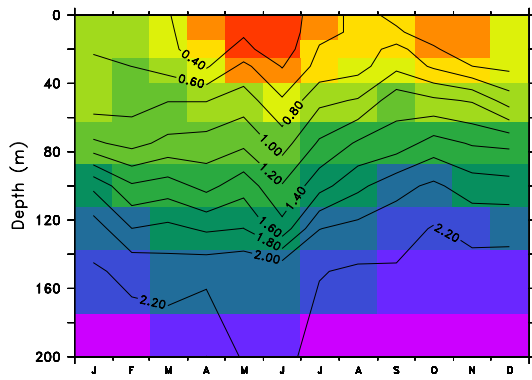
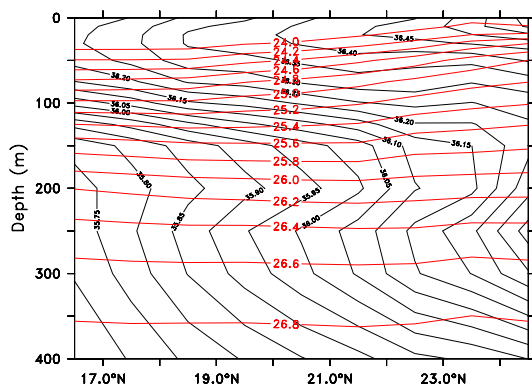(a) Northern part; average WOA09: 60°-66°E and 19°-23°N
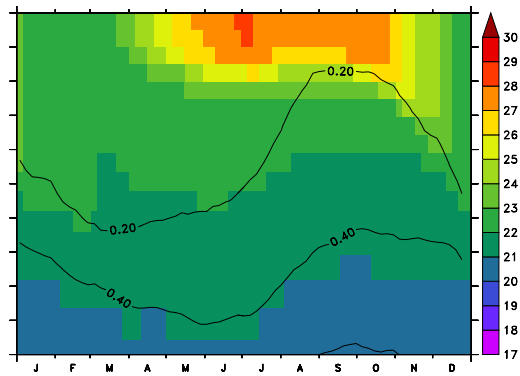
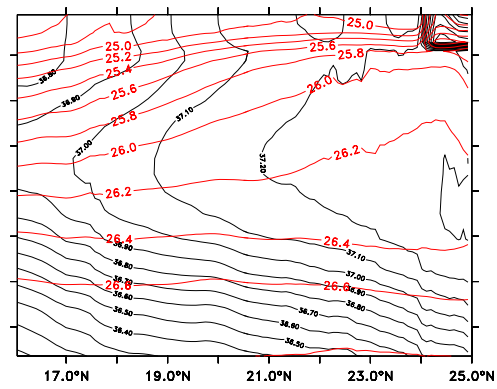(b) Northern part; average GFDL CM2.6 (year 197): 60°-66°E and 19°-23°N
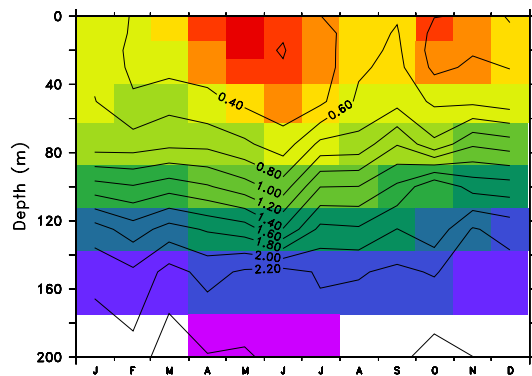
(c) Southern part; average WOA09: 60°-66°E and 19°-23°N
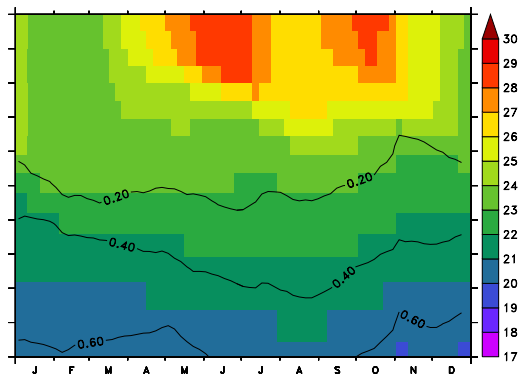
(d) Southern part; average GFDL CM2.6 (year 197): 60°-66°E and 19°-23°N
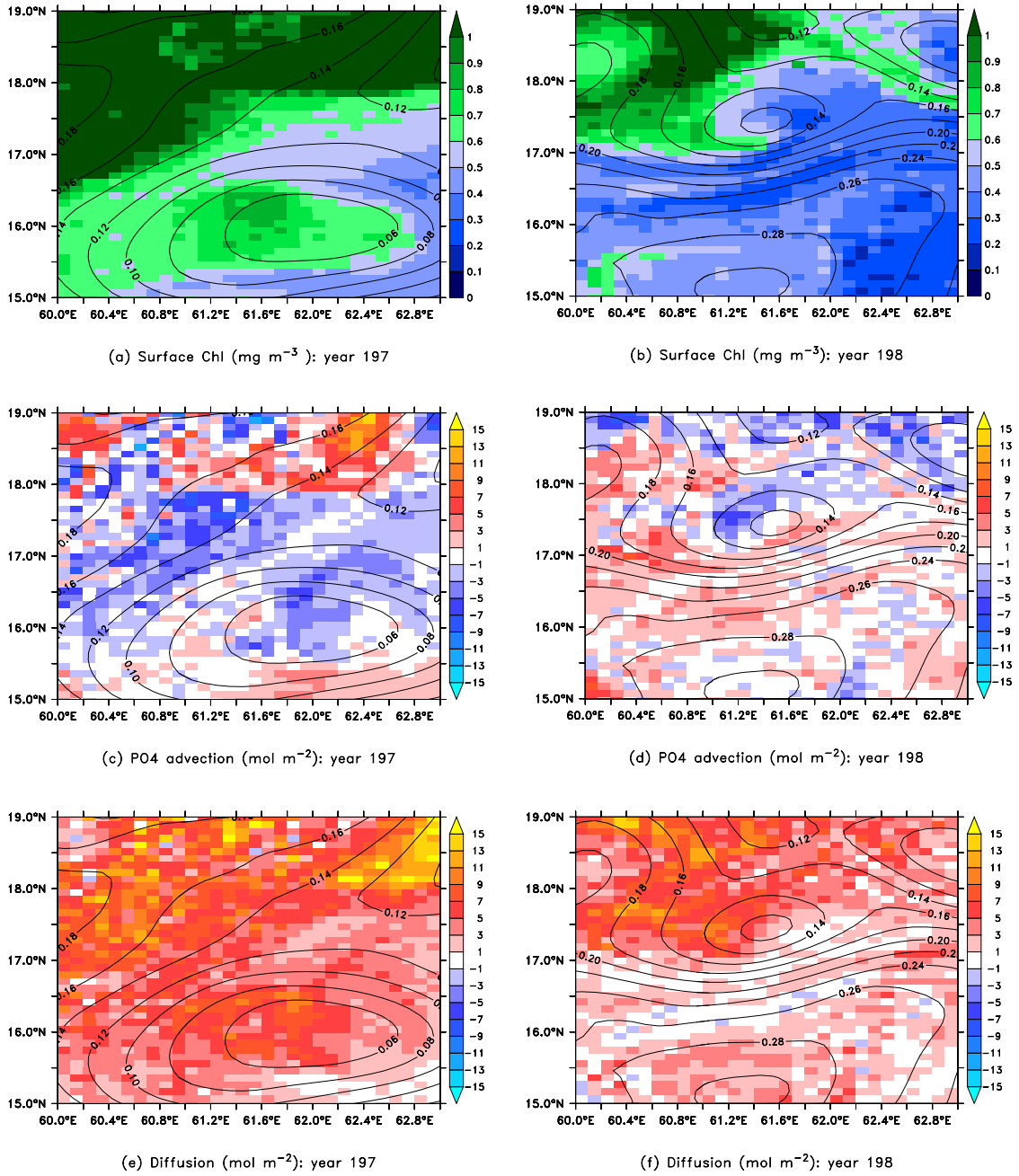
(e) WOA09 results: 60°-66°E

(f) GFDL CM2.6 (year 197): 60°-66°E

936

Figure 13. (a-d) Seawater temperature (colors, °C) and Phosphate (PO$_4$) concentration (contours, μM) for the northern (top row) and southern (middle row) parts of the central Arabian Sea. ; (e-f) yearly averaged subsurface distribution of salinity (black contours) and potential density (red contours). Left-hand column shows observations with the Persian Gulf plume centered at 300m, right-hand column results from CM2.6 model with a much broader mixing of salinity over the top 200m.

943

(a) Surface Chl (mg m^{-3}): year 197

(b) Surface Chl (mg m^{-3}): year 198

(c) PO4 advection (mol m^{-2}): year 197

(d) PO4 advection (mol m^{-2}): year 198

(e) Diffusion (mol m^{-2}): year 197

(f) Diffusion (mol m^{-2}): year 198

944

Figure 14. Surface chlorophyll in mg/m^3. (a-b), Advective flux of phosphate to top 50m in mol/m^2 (c-d,colors), and diffusive flux of phosphate in mol/m^2 (e-f, colors) with sea surface height (contours in m, contour interval 0.02m) for eddy E1 (63°-66°E, 15°-18°N) for the month of December during the two CM2.6 model years 197 and 198.

949

950

951
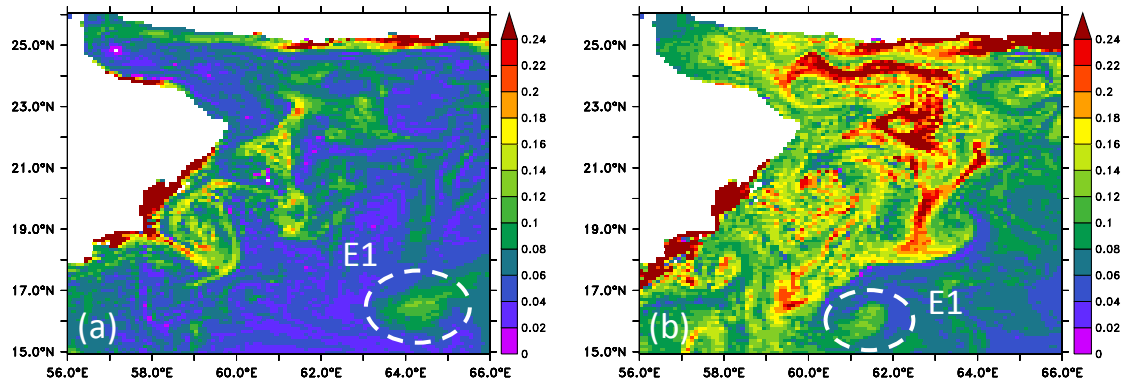
Figure 15. (a), (b) : CM2.6 (miniBLING) PO$_4$ on 9 November and 28 December of year 197.(56°–66° E, 15° –26° N).